Available online at www.sciencedirect.com
ScienceDirect
Comput. Methods Appl. Mech. Engrg. 279 (2014) 554–578
Computer methods in applied mechanics and engineering
www.elsevier.com/locate/cma

Stabilized stress–velocity–pressure finite element formulations of the Navier–Stokes problem for fluids with non-linear viscosity

Ernesto Castillo, Ramon Codina*

Universitat Politècnica de Catalunya, Jordi Girona 1-3, Edifici C1, 08034 Barcelona, Spain

Received 23 September 2013; received in revised form 6 April 2014; accepted 5 July 2014
Available online 14 July 2014

Highlights

- Detailed description of the mixed three-field formulation of the incompressible Navier–Stokes equations, including non-Newtonian fluids.
- Derivation of mixed stabilized finite element methods for the three-field problem presented.
- Description of implementation issues of the formulations proposed.
- Numerical testing of the resulting formulation through numerous examples.

Abstract

The three-field (stress–velocity–pressure) mixed formulation of the incompressible Navier–Stokes problem can lead to two different types of numerical instabilities. The first is associated with the incompressibility and loss of stability in the calculation of the stress field, and the second with the dominant convection. The first type of instabilities can be overcome by choosing an interpolation for the unknowns that satisfies the appropriate inf–sup conditions, whereas the dominant convection requires a stabilized formulation in any case. This paper proposes two stabilized schemes of Sub-Grid Scale (SGS) type, differing in the definition of the space of the sub-grid scales, and both allowing to use the same interpolation for the variables $\boldsymbol{\sigma}$–$\boldsymbol{u}$–p (deviatoric stress, velocity and pressure), even in problems where the convection component is dominant and the velocity–stress gradients are high. Another aspect considered in this work is the non-linearity of the viscosity, modeled with constitutive models of quasi-Newtonian type. This paper includes a description of the proposed methods, some of their implementation issues and a discussion about benefits and drawbacks of a three-field formulation. Several numerical examples serve to justify our claims.
© 2014 Elsevier B.V. All rights reserved.

Keywords: Incompressible flows; Three-field formulation; Mixed finite element methods; Stabilized formulations; Non-Newtonian fluids

1. Introduction

Fluids, depending on their behavior under the action of shear-stress, can be classified as Newtonian and non-Newtonian. The last group is predominant in the petroleum industry, in chemical–pharmaceutical processes and in

* Corresponding author. Tel.: +34 934016486.
E-mail addresses: ecastillo@cimne.upc.edu (E. Castillo), ramon.codina@upc.edu (R. Codina).

http://dx.doi.org/10.1016/j.cma.2014.07.003
0045-7825/© 2014 Elsevier B.V. All rights reserved.

food products [1–4]. The non-Newtonian behavior is caused by the complex microstructure present in these fluids, in some cases originated by a mixture of different components, which in turn can be found in different states. For example, blood is a complex fluid composed of red cells, white cells, platelets and plasma, which at different shear stresses can pass from a fluid exhibiting Newtonian behavior to one exhibiting pseudoplastic non-Newtonian behavior in high shear stress ranges [5].

There are specific texts devoted to rheology [6,7] where we can find detailed descriptions of classical models. The simplest of them of quasi-Newtonian type is the Ostwald–de Waele or power-law model. More specific for example is the Walburn–Schneck model [8] for modeling blood flow, which includes among its parameters the amount of hematocrit H or fraction of red cells in the blood. The polymeric models consider other factors that modify the viscosity, such as the molecular weight, the polymeric concentration and the changes in the shape of the polymer chain [9]. Within the quasi-Newtonian classical models, the four parameter Carreau model and the five parameter Carreau–Yasuda model allows one to constrain the limit values in the viscosity when the power-law model predicts non-physical values at high and low shear stresses.

In this work we are interested in the finite element approximation of this type of problems. In particular, we aim to explore the possibilities and benefits of using a three-field formulation, having as unknowns the deviatoric stress, the velocity and the pressure. These mixed approximations can lead to different types of numerical instabilities inherent to the mathematical structure of the equations to be solved when the classical Galerkin approach is used. On the one hand, pressure and velocity are out of control unless appropriate inf–sup conditions are satisfied by the interpolation spaces. Conditions of this type need to be fulfilled also for the velocity and stress interpolation spaces. On the other hand, small viscosity values can lead to the classical instabilities found in convection dominated flows.

Referring to the compatibility conditions (see e.g. [10]), for the three-field approximation they consist of two restrictions, one between pressure and velocity and the other between velocity and stress [11]. These two restrictions reduce the choices of stable finite element spaces that allow one to discretize the unknowns. For example, in [12,13] it is shown how to design elements that satisfy the inf–sup condition between velocities and stresses through the addition of bubble functions. Another way to satisfy this restriction is using discontinuous finite element spaces for the stress, as shown in [14]. In the viscoelastic fluid context, a well-known stable interpolation in the two-dimensional case consists of using biquadratic elements for the velocity field, bilinear pressure interpolation and a multi-bilinear interpolation for the stresses, which is the popular Marchal–Crochet element [15]. The mathematical analysis of this element can be found in [16]. It is a clear example of the difficulties to satisfy the inf–sup conditions associated to the three-field formulation of flow problems.

When convection becomes dominant, it is necessary to use a stabilized formulation in any case. Among the methods that serve this purpose one can use the Streamline-Upwind/Petrov–Galerkin (SUPG) method [17], the Galerkin-Least Square (GLS) method [18], the Characteristics Galerkin method [19] or the Taylor–Galerkin method [20] (see [21]).

The two stabilized formulations proposed in this work are framed in the context of sub-grid scale (SGS) methods (also termed variational multi-scale methods) introduced by Hughes et al. [22] for the scalar convection–diffusion–reaction problem, and extended later to the vectorial Stokes problem in [23], where the space of the sub-grid scales is taken as orthogonal to the finite element space. The purpose of the present paper is to extend and test numerically the formulation presented in [11] for the Stokes problem with constant viscosity to a three-field formulation $\boldsymbol{\sigma}$–$\boldsymbol{u}$–p (deviatoric stress, velocity and pressure) of the Navier–Stokes problem with non-linear viscosity.

The starting point of a sub-grid scale approach is to split the unknowns of the problem into two components, namely, the component that can be approximated by the finite element mesh and the unresolvable one, called sub-grid scale or simply sub-scale in what follows. The latter needs to be approximated in a simple manner in terms of the former, so as to capture its main effect and yield a stable formulation for the finite element unknown. The number of degrees of freedom is therefore the same as for the Galerkin method. There are different ways to approximate the sub-scale and, in particular, to choose the (finite dimensional) space where it is taken. In this paper we will describe two formulations which precisely differ in this choice. In the first one, it will be equal to the space of finite element residuals (in a sense to be made precise in what follows), whereas in the second the space for the sub-scales will be taken as orthogonal to the finite element space. Both formulations will allow one to deal with the instabilities of the three-field formulation described earlier. There will be no need to meet the inf–sup conditions for the interpolation spaces and it will be possible to solve convection dominated problems.

We have performed a rather complete numerical testing of the formulations presented. The numerical results shown in this work can be separated into four groups. The first (Section 4.1) corresponds to the study of the convergence of

the formulations proposed for the stationary case with non-linear viscosity, more precisely for a power-law fluid with a power-law index in the range $0.5 \leq n \leq 1.5$ and in the range of Reynolds number $0.3 \leq \mathrm{Re} \leq 400$, using linear and quadratic triangular elements. To perform this test we manufacture the solution by introducing a force term computed with a predetermined stress–velocity–pressure solution. The second group of results corresponds to a stationary lid-driven square cavity, where the fluid is subject to a parallel flow and it is modeled by the Ostwald–de Waele constitutive model, for a power-law index in the range $0.5 \leq n \leq 1.5$ and with a regime of flow in the range of $100 \leq \mathrm{Re} \leq 5000$. We compare our results with those published by Mendu and Das [24]. The third group of numerical results corresponds to the classical problem of the flow over a cylinder for a highly convected case ($\mathrm{Re} = 140$) of a fluid with non-linear viscosity in the power-law range of $0.4 \leq n \leq 1.8$. We compare some characteristic parameters of the flow obtained with our formulation, like the Strouhal number (St), the drag coefficient ($\mathrm{C_D}$) and the lift coefficient ($\mathrm{C_L}$), with those published by Patnana et al. [25]. This example closes the evaluation of the two formulations in the cases of nonlinear viscosity and dominant convection, in stationary and transient problems. The section with numerical examples concludes with an analysis of the shear stresses over walls computed with the three-field formulation and a classical two-field (velocity–pressure) one, showing the accuracy improvement obtained with the former. This suggests the interest of using the three-field approach in situations in which the accurate evaluation of the shear stresses may be crucial, such as in blood flow or in some fluid–structure interaction problems. Furthermore, it gives confidence in its use in more complex rheological behavior, such as that of viscoelastic fluids, in which the introduction of stresses as unknowns is almost a must.

The work is organized as follows. Section 2 contains the presentation of the problem, with the three-field continuous Navier–Stokes equations, its variational form, the description of some non-Newtonian constitutive models and the straightforward Galerkin finite element discretization in space and finite difference discretization in time. Section 3 presents our stabilized finite element approach, with the description of the general idea and its application to the present problem. The linearization of the problem is also discussed. Section 4 contains the numerical results described above and, finally, in Section 5 conclusions are summarized.

2. The Navier–Stokes problem in a three-field formulation

2.1. Initial and boundary value problem

Let Ω be the computational domain of $\mathbb{R}^{\mathrm{d}}$ ($d = 2$ or 3) occupied by the fluid in the time interval $[0, T]$, assumed to be bounded and polyhedral, and let $\partial\Omega$ be its boundary. The incompressible Navier–Stokes equations formulated in terms of stress–velocity–pressure can be written as:

$$
\begin{aligned}
&\rho\frac{\partial \boldsymbol{u}}{\partial t} - \nabla\cdot\boldsymbol{\sigma} + \rho\boldsymbol{u}\cdot\nabla\boldsymbol{u} + \nabla p = \boldsymbol{f} \quad \text{in } \Omega,\ t \in]0, T[,\\
&\nabla\cdot\boldsymbol{u} = 0 \quad \text{in } \Omega,\ t \in]0, T[,\\
&\frac{1}{2\eta}\boldsymbol{\sigma} - \nabla^s\boldsymbol{u} = \boldsymbol{0} \quad \text{in } \Omega,\ t \in]0, T[,
\end{aligned}
$$

where $\boldsymbol{u}$ is the velocity field, p the pressure, $\boldsymbol{\sigma}$ the deviatoric component of the stress field, $\boldsymbol{f}$ the vector of body forces, η corresponds to the apparent viscosity of the fluid, which in the Newtonian case is identical to the dynamic viscosity (μ), ρ is the fluid density and $\nabla^s\boldsymbol{u}$ is the symmetrical part of $\nabla\boldsymbol{u}$.

The equations above need to be solved together with initial conditions of the form $\boldsymbol{u} = \boldsymbol{u}^0$ and appropriate boundary conditions. For the sake of simplicity in the exposition, we will consider homogeneous boundary conditions $\boldsymbol{u} = \boldsymbol{0}$ on $\partial\Omega$.

2.2. The variational form

In order to write the weak form of the problem, let us introduce some notation. As usual, the space of square integrable functions in a domain Ω is denoted by $L^2(\Omega)$, while the space of functions whose first derivatives are square integrable is denoted by $H^1(\Omega)$. The space $H^1_0(\Omega)$ consists of functions in $H^1(\Omega)$ vanishing on $\partial\Omega$. Using this notation, the finite element spaces used in the continuous three-field problem are $L^2(0,\ T;\ \boldsymbol{\mathcal{V}}_0)$ for the velocity field, $\mathcal{D}'(0,\ T;\ Q)$ for the pressure, and $\mathcal{D}'(0,\ T;\ \boldsymbol{\Upsilon})$ for the stress field, where $\boldsymbol{\mathcal{V}}_0 = H^1_0(\Omega)^d$, $Q = L^2(\Omega)/\mathbb{R}$, $\boldsymbol{\Upsilon} =$

$L^2(\Omega)^{d\times d}_{\text{sym}}$ (symmetric second order tensors with square-integrable components) and $\mathcal{D}'$ is used to denote distributions in time.

For constant viscosity, the weak form of the problem consists in finding $\boldsymbol{U} = [\boldsymbol{u}, p, \boldsymbol{\sigma}] \in \boldsymbol{X}_T = L^2(0, T; \boldsymbol{\mathcal{V}}_0) \times \mathcal{D}'(0, T; Q) \times \mathcal{D}'(0, T; \boldsymbol{\Upsilon})$ such that:

$$\left(\rho\frac{\partial \boldsymbol{u}}{\partial t}, \boldsymbol{v}\right) + \left(\nabla^s \boldsymbol{v}, \boldsymbol{\sigma}\right) + \langle \rho\boldsymbol{u}\cdot\nabla\boldsymbol{u}, \boldsymbol{v}\rangle - (p, \nabla\cdot\boldsymbol{v}) = \langle \boldsymbol{f}, \boldsymbol{v}\rangle,$$
$$(q, \nabla\cdot\boldsymbol{u}) = 0,$$
$$\left(\frac{1}{2\eta}\boldsymbol{\sigma}, \boldsymbol{\tau}\right) - \left(\nabla^s\boldsymbol{u}, \boldsymbol{\tau}\right) = 0,$$

for all $\boldsymbol{V} = [\boldsymbol{v}, q, \boldsymbol{\tau}] \in \boldsymbol{X} = \boldsymbol{\mathcal{V}}_0 \times Q \times \boldsymbol{\Upsilon}$, where $(\cdot,\cdot)$ stands for the L^2 inner product and $\langle\cdot,\cdot\rangle$ is the integral of the product of the functions in the two arguments, whenever it makes sense. In particular, it is the duality pairing between $\boldsymbol{\mathcal{V}}_0$ and its dual $(H^{-1}(\Omega))^d$, where $\boldsymbol{f}$ is assumed to belong.

In compact form, the problem can be written as:

$$\left(\rho\frac{\partial \boldsymbol{u}}{\partial t}, \boldsymbol{v}\right) + B(\boldsymbol{U}, \boldsymbol{V}) = \langle \boldsymbol{f}, \boldsymbol{v}\rangle, \tag{1}$$

where

$$B(\boldsymbol{U}, \boldsymbol{V}) = \left(\nabla^s\boldsymbol{v}, \boldsymbol{\sigma}\right) + \langle \rho\boldsymbol{u}\cdot\nabla\boldsymbol{u}, \boldsymbol{v}\rangle - (p, \nabla\cdot\boldsymbol{v}) + (q, \nabla\cdot\boldsymbol{u}) + \left(\frac{1}{2\eta}\boldsymbol{\sigma}, \boldsymbol{\tau}\right) - \left(\nabla^s\boldsymbol{u}, \boldsymbol{\tau}\right).$$

Eq. (1) needs to be completed with the initial condition satisfied in a weak sense.

In the case of nonlinear viscosities, more regularity on the stresses and the velocities might be required depending on the constitutive model. This is however outside the scope of this work.

2.3. Non-Newtonian models

In many fluids the viscosity may be dependent on the rate of strain as well as on the state variables, such as temperature and pressure or total deformation (see for example [26]). Typical cases can be found in biological fluids (blood, saliva, synovial fluid), adhesives, food products (pureed fruits/vegetables, sauces), greases and lubricants, polymers and molten metals, among others. The non-Newtonian models abound in the literature and the formulations can vary from a simple two-parameter power-law model to complex models designed for specific fluids. In the simplest case, the constitutive law of a non-Newtonian fluid is written in terms of the second invariant of the strain rate tensor, which we will denote as I_2.

In the present work, two non-Newtonian models have been implemented to characterize the non-linear viscosity character, both based on I_2. These are the two-parameter power law model and the five-parameter Carreau–Yasuda model, respectively given by

$$\eta = m\left(\frac{I_2}{2}\right)^{\frac{n-1}{2}}, \tag{2}$$

$$\eta = \mu_\infty + (\mu_0 - \mu_\infty)\left(1 + \left(\lambda\sqrt{I_2}\right)^b\right)^{\frac{n-1}{b}}, \tag{3}$$

where

$$I_2 = 2(\dot{\boldsymbol{\varepsilon}} : \dot{\boldsymbol{\varepsilon}}), \qquad \dot{\boldsymbol{\varepsilon}} = \frac{1}{2}\left[(\nabla\boldsymbol{u}) + (\nabla\boldsymbol{u})^{\mathrm{T}}\right] =: \nabla^s\boldsymbol{u}.$$

In (2)–(3), m represents the consistency index, n the power-law index, μ_0 and μ_∞ the limit values of the viscosity in the Carreau–Yasuda model, and λ and b are constants of this model. When $b = 2$, the Carreau–Yasuda model is the classical Carreau model.

The two-parameter power-law model is the simplest of the models that allow one to introduce a nonlinear relationship between viscosity and shear rate. The major drawback of this model is seen at low and high shear rates, where

the apparent viscosity value can tend to singular values. With respect to this problem, the Carreau–Yasuda model is superior, allowing to control the range of viscosities, with the disadvantage of requiring a larger number of parameters to be implemented.

Even though we will use the described models in the numerical examples, the stabilized formulation presented in Section 3 is completely general and any generalized Newtonian model can be easily implemented.

2.4. Galerkin finite element discretization and time discretization

The standard Galerkin approximation for the variational problem defined by (1) can be performed by considering a finite element partition $\mathcal{T}_h$ of the domain Ω. The diameter of an element domain $K \in \mathcal{T}_h$ is denoted by h_K and the diameter of the element partition is defined by $h = \max\{h_K \mid K \in \mathcal{T}_h\}$. From $\mathcal{T}_h$, we can construct conforming finite element spaces, $\boldsymbol{\mathcal{V}}_{h,0} \subset \boldsymbol{\mathcal{V}}_0$, $Q_h \subset Q$ and $\boldsymbol{\Upsilon}_h \subset \boldsymbol{\Upsilon}$ in the usual manner. If $\boldsymbol{X}_h = \boldsymbol{\mathcal{V}}_{h,0} \times Q_h \times \boldsymbol{\Upsilon}_h$ and $\boldsymbol{U}_h = [\boldsymbol{u}_h, p_h, \boldsymbol{\sigma}_h]$, the Galerkin finite element approximation consists in finding $\boldsymbol{U}_h \in C^0(0, T; \boldsymbol{X}_h)$ such that

$$\left(\rho \frac{\partial \boldsymbol{u}_h}{\partial t}, \boldsymbol{v}_h\right) + B(\boldsymbol{U}_h, \boldsymbol{V}_h) = \langle \boldsymbol{f}, \boldsymbol{v}_h \rangle, \tag{4}$$

for all $\boldsymbol{V}_h = [\boldsymbol{v}_h, q_h, \boldsymbol{\tau}_h] \in \boldsymbol{X}_h$.

The term involving the time derivative can be discretized in different ways. A possible option is to use a space–time finite element formulation, although we will use the most common option of discretizing in time using finite differences. In particular, we have implemented the first order backward differencing (BE or BDF1) and the second order backward differencing (BDF2) schemes, based respectively on the approximations

$$\left.\frac{\partial \boldsymbol{u}_h}{\partial t}\right|^{j+1} = \frac{\boldsymbol{u}_h^{j+1} - \boldsymbol{u}_h^{j}}{\delta t} + O(\delta t),$$
$$\left.\frac{\partial \boldsymbol{u}_h}{\partial t}\right|^{j+1} = \frac{3\boldsymbol{u}_h^{j+1} - 4\boldsymbol{u}_h^{j} + \boldsymbol{u}_h^{j-1}}{2\delta t} + O\left(\delta t^2\right).$$

In both cases, δt corresponds to the size of a uniform partition of the time interval $[0, T]$, while $O(\cdot)$ represents the approximation order of the scheme. The superscript indicates the time step where the variable is being approximated, so that $\boldsymbol{u}_h^j$ is an approximation to $\boldsymbol{u}_h$ at time $t^j = j\delta t$.

So far, no conditions have been imposed on the choice of the finite element spaces. However, there are restrictions that must be satisfied explicitly in the discrete formulation used. To see this, consider the stationary Stokes problem with constant viscosity, which can be written as: find $\boldsymbol{U}_h = [\boldsymbol{u}_h, p_h, \boldsymbol{\sigma}_h] \in \boldsymbol{X}_h$ such that

$$B_0(\boldsymbol{U}_h, \boldsymbol{V}_h) = \langle \boldsymbol{f}, \boldsymbol{v}_h \rangle,$$

for all $\boldsymbol{V}_h = [\boldsymbol{v}_h, q_h, \boldsymbol{\tau}_h] \in \boldsymbol{X}_h$, with

$$B_0(\boldsymbol{U}_h, \boldsymbol{V}_h) = \left(\nabla^s \boldsymbol{v}_h, \boldsymbol{\sigma}_h\right) - (p_h, \nabla \cdot \boldsymbol{v}_h) + (q_h, \nabla \cdot \boldsymbol{u}_h) + \left(\frac{1}{2\mu}\boldsymbol{\sigma}_h, \boldsymbol{\tau}_h\right) - \left(\nabla^s \boldsymbol{u}_h, \boldsymbol{\tau}_h\right). \tag{5}$$

Taking $\boldsymbol{V}_h = \boldsymbol{U}_h$ it is easily seen that the Galerkin formulation only provides control over the stress field:

$$B_0(\boldsymbol{U}_h, \boldsymbol{U}_h) = \frac{1}{2\mu} \|\boldsymbol{\sigma}_h\|^2.$$

The three-field Stokes problem has been studied by a large number of authors (see for example [27,28]). It can be shown that the classical inf–sup condition:

$$\inf_{\boldsymbol{U}_h \in \boldsymbol{X}_h} \sup_{\boldsymbol{V}_h \in \boldsymbol{X}_h} \frac{B_0(\boldsymbol{U}_h, \boldsymbol{V}_h)}{\|\boldsymbol{U}_h\|_{\boldsymbol{X}} \|\boldsymbol{V}_h\|_{\boldsymbol{X}}} \geq \beta$$

is not satisfied for any positive constant β, unless the following two conditions hold:

$$\inf_{q_h \in Q_h} \sup_{\boldsymbol{v}_h \in \boldsymbol{V}_h} \frac{(q_h, \nabla \cdot \boldsymbol{v}_h)}{\|q_h\|_Q \|\boldsymbol{v}_h\|_{\boldsymbol{V}}} \geq C_1, \tag{6}$$

$$\inf_{\boldsymbol{v}_h \in \boldsymbol{V}_h} \sup_{\boldsymbol{\tau}_h \in \boldsymbol{\Upsilon}_h} \frac{(\boldsymbol{\tau}_h, \nabla^s \boldsymbol{v}_h)}{\|\boldsymbol{\tau}_h\|_{\boldsymbol{\Upsilon}} \, \|\boldsymbol{v}_h\|_{\boldsymbol{V}}} \geq C_2, \tag{7}$$

where C_1 and C_2 represent two positive constants independent of h, while $\|\cdot\|_Y$ stands for the appropriate norm in space Y. A stable numerical formulation is obtained if the finite element spaces satisfy (6)–(7). However, from the numerical point of view, the spaces that fulfill these conditions are limited, particularly when the problem needs to be solved in three dimensions. The alternative is to use a stabilized formulation allowing any interpolation for the variables. In general, a stabilized formulation consists of replacing (5) by another bilinear form B_h, possibly mesh dependent, with enhanced stability properties. In the Navier–Stokes equations, it has to be also capable of dealing with the instabilities generated in the case of dominant convection. The two stabilized formulations presented below satisfy these conditions.

3. Design of a stable finite element formulation for the three-field Navier–Stokes problem

In the following we present two stabilized formulations for the three-field Navier–Stokes problem analyzed. Both formulations are based on the variational multi-scale approach introduced by Hughes et al. [22] for the scalar convection–diffusion problem. The basic idea is to approximate the effect of the components of the solution of the continuous problem that cannot be resolved by the finite element mesh. Here we present the general idea in the case of a general nonlinear evolution problem, and then particularize it to the problem of interest. The presentation is formal, avoiding technicalities and trying to describe the essential ideas and simplifications.

Consider a differential equation of the form:

$$\boldsymbol{M}(\boldsymbol{U}) \frac{\partial \boldsymbol{U}}{\partial t} + \mathcal{L}(\boldsymbol{U}, \boldsymbol{U}) = \boldsymbol{F}, \tag{8}$$

where $\boldsymbol{U}$ contains the unknowns of the problem (which in our particular case are $[\boldsymbol{u}, p, \boldsymbol{\sigma}]$), $\mathcal{L}(\boldsymbol{U}, \cdot)$ corresponds to an operator associated with the specific problem assumed to be linear in the second argument, $\boldsymbol{M}(\boldsymbol{U})$ is a mass matrix and $\boldsymbol{F}$ a force vector.

The weak form of the generic problem (8) can be formally written as

$$\left(\boldsymbol{M}(\boldsymbol{U}) \frac{\partial \boldsymbol{U}}{\partial t}, \boldsymbol{V}\right) + \langle \mathcal{L}(\boldsymbol{U}, \boldsymbol{U}), \boldsymbol{V} \rangle = \langle \boldsymbol{F}, \boldsymbol{V} \rangle, \tag{9}$$

for an appropriate "duality" and considering $\boldsymbol{V}$ as a test function. The boundary conditions of the problem have to be taken into account, and are understood to be incorporated in the duality $\langle \cdot, \cdot \rangle$. Likewise, when considering finite element functions the duality has to be understood as the element-wise integral with appropriate inter-element jumps.

3.1. The sub-scale concept

The basic idea of the formulation applied to the generic problem is to split the unknown as $\boldsymbol{U} = \boldsymbol{U}_h + \boldsymbol{U}'$, where $\boldsymbol{U}_h \in \boldsymbol{X}_h$ is the component of the solution that belongs to the finite element space and $\boldsymbol{U}' \in \boldsymbol{X}'$ is the remainder, referred to as sub-grid scale or sub-scale. The spaces $\boldsymbol{X}_h$ and $\boldsymbol{X}'$ are such that $\boldsymbol{X} = \boldsymbol{X}_h \bigoplus \boldsymbol{X}'$. Under the above considerations, the original problem (9) is exactly equivalent to:

$$\left(\boldsymbol{M}(\boldsymbol{U}) \frac{\partial \boldsymbol{U}}{\partial t}, \boldsymbol{V}_h\right) + \langle \mathcal{L}(\boldsymbol{U}, \boldsymbol{U}), \boldsymbol{V}_h \rangle = \langle \boldsymbol{F}, \boldsymbol{V}_h \rangle \quad \forall \boldsymbol{V}_h \in \boldsymbol{X}_h, \tag{10}$$

$$\left(\boldsymbol{M}(\boldsymbol{U}) \frac{\partial \boldsymbol{U}}{\partial t}, \boldsymbol{V}'\right) + \left\langle \mathcal{L}(\boldsymbol{U}, \boldsymbol{U}), \boldsymbol{V}' \right\rangle = \left\langle \boldsymbol{F}, \boldsymbol{V}' \right\rangle \quad \forall \boldsymbol{V}' \in \boldsymbol{X}'. \tag{11}$$

In essence, the goal of all SGS methods, including the approximation of the sub-scale with bubble functions, is to approximate $\boldsymbol{U}'$ in one way or another and end up with a problem for $\boldsymbol{U}_h$ alone.

3.2. General approach of the sub-scale stabilized formulation

There are different approximations for the sub-scale component $\boldsymbol{U}'$ that allow one to write it as a function of the finite element component, $\boldsymbol{U}_h$.

We call the sub-scales *dynamic* if their temporal derivative is taken into account, whereas if it is neglected we call them *quasi-static*. Another possible simplification is to consider that they vanish on the inter-element boundaries, as it is done for example when bubble functions are used to approximate the sub-scales. We will assume this, although this restriction could be relaxed (see [11]). A third possible simplification, explained in more detail below, is to neglect the sub-scale effect on the non-linear terms of the equation.

Apart from the simplifications described, another important ingredient in the construction of the stabilized formulation is the choice of the space where the sub-scales belong. The most common choice is to take it equal to the space generated by the operator associated with the problem, applied to the finite element space [29]. Another possibility is to take it orthogonal to the finite element space, that is, $\boldsymbol{X}' = \boldsymbol{X}_h^{\perp}$, resulting in the so called orthogonal sub-scales (OSS) method [30].

Eqs. (10)–(11), after an appropriate integration by parts, can be written as follows:

$$\left(\boldsymbol{M}(\boldsymbol{U})\frac{\partial \boldsymbol{U}}{\partial t}, \boldsymbol{V}_h\right) + \langle \mathcal{L}\left(\boldsymbol{U}, \boldsymbol{U}_h\right), \boldsymbol{V}_h\rangle + \left\langle \boldsymbol{U}', \mathcal{L}^*\left(\boldsymbol{U}, \boldsymbol{V}_h\right)\right\rangle = \langle \boldsymbol{F}, \boldsymbol{V}_h\rangle \quad \forall \boldsymbol{V}_h \in \boldsymbol{X}_h, \tag{12}$$

$$\left(\boldsymbol{M}(\boldsymbol{U})\frac{\partial \boldsymbol{U}}{\partial t}, \boldsymbol{V}'\right) + \left\langle \mathcal{L}\left(\boldsymbol{U}, \boldsymbol{U}_h\right), \boldsymbol{V}'\right\rangle + \left\langle \boldsymbol{U}', \mathcal{L}^*\left(\boldsymbol{U}, \boldsymbol{V}'\right)\right\rangle = \left\langle \boldsymbol{F}, \boldsymbol{V}'\right\rangle \quad \forall \boldsymbol{V}' \in \boldsymbol{X}', \tag{13}$$

where we have introduced the formal adjoint $\mathcal{L}^*(\boldsymbol{U}, \cdot)$ of operator $\mathcal{L}(\boldsymbol{U}, \cdot)$, which is defined through the relationship

$$\langle \mathcal{L}\left(\boldsymbol{U}, \boldsymbol{W}\right), \boldsymbol{V}\rangle = \left\langle \boldsymbol{W}, \mathcal{L}^*\left(\boldsymbol{U}, \boldsymbol{V}\right)\right\rangle,$$

for all $\boldsymbol{U}$, $\boldsymbol{W}$, $\boldsymbol{V} \in \boldsymbol{X}$. Again, the duality might involve inter-element jump terms when finite element functions are considered. However, if these inter-element terms are neglected and P' denotes the L^2 projection onto the space of sub-scales, Eq. (13) can be formally written as

$$P'\left[\boldsymbol{M}(\boldsymbol{U})\frac{\partial \boldsymbol{U}'}{\partial t} + \mathcal{L}\left(\boldsymbol{U}, \boldsymbol{U}'\right)\right] = P'\left[\boldsymbol{R}_{\boldsymbol{U}}\right],$$

where $\boldsymbol{R}_{\boldsymbol{U}}$ represents the residual of the finite element approximation, that is to say,

$$\boldsymbol{R}_{\boldsymbol{U}} = \boldsymbol{F} - \boldsymbol{M}(\boldsymbol{U})\frac{\partial \boldsymbol{U}_h}{\partial t} - \mathcal{L}\left(\boldsymbol{U}, \boldsymbol{U}_h\right).$$

At this point additional approximations are required and different methods may be devised according to the approximations chosen. A particular case of the sub-scale method described above is an algebraic approximation of the sub-scales [31]. The approximation of the problem in this case is:

$$\mathcal{L}\left(\boldsymbol{U}, \boldsymbol{U}'\right) \approx \boldsymbol{\alpha}^{-1}\left(\boldsymbol{U}\right)\boldsymbol{U}',$$

where $\boldsymbol{\alpha}^{-1}\left(\boldsymbol{U}\right)$ is a matrix defined within each element domain that has to be determined. We shall refer to it as the matrix of stabilization parameters.

With the above approximation, for an adequate projection onto the sub-scale space $P', \boldsymbol{U}'$ needs to be calculated from the following ordinary nonlinear differential equation in each element:

$$\boldsymbol{M}(\boldsymbol{U}_h + \boldsymbol{U}')\frac{\partial \boldsymbol{U}'}{\partial t} + \boldsymbol{\alpha}^{-1}\left(\boldsymbol{U}_h + \boldsymbol{U}'\right)\boldsymbol{U}' = P'\left[\boldsymbol{F} - \boldsymbol{M}(\boldsymbol{U}_h + \boldsymbol{U}')\frac{\partial \boldsymbol{U}_h}{\partial t} - \mathcal{L}\left(\boldsymbol{U}_h + \boldsymbol{U}', \boldsymbol{U}_h\right)\right], \tag{14}$$

where we have assumed for simplicity that the terms on the left-hand side are in the space of sub-scales.

It is important to note that the calculation of $\boldsymbol{U}'$ needs to be made at the integration points, that is to say, Eq. (14) is in fact a nonlinear ordinary differential equation.

3.3. Stabilized formulation applied to the three-field Navier–Stokes problem

Let us apply the general procedure described to the three-field form of the incompressible Navier–Stokes equations. The key point is the approximation of matrix $\boldsymbol{\alpha}(\boldsymbol{U})$. We shall not motivate it here, but simply use the same heuristic arguments as in [11]. Taking this matrix diagonal, of the form $\boldsymbol{\alpha} = \mathrm{diag}(\alpha_1 \boldsymbol{I}_{\boldsymbol{u}}, \alpha_2, \alpha_3 \boldsymbol{I}_{\boldsymbol{\sigma}})$, with $\boldsymbol{I}_{\boldsymbol{u}}$ and $\boldsymbol{I}_{\boldsymbol{\sigma}}$ the identity

matrices on velocities and stresses, respectively, Eq. (14) reads

$$\rho\frac{\partial \boldsymbol{u}'}{\partial t}+\frac{1}{\alpha_1}\boldsymbol{u}'=P'\left(\boldsymbol{R_u}\right), \tag{15}$$

$$\frac{1}{\alpha_2}p'=P'\left(R_p\right), \tag{16}$$

$$\frac{1}{\alpha_3}\boldsymbol{\sigma}'=P'\left(\boldsymbol{R_\sigma}\right), \tag{17}$$

where $\boldsymbol{R_u}$ corresponds to the residual of the momentum equation, R_p the residual of the continuity equation and $\boldsymbol{R_\sigma}$ the residual of the constitutive equation.

Problem (15)–(17) (with initial conditions for the sub-scale velocity) is in fact a differential–algebraic system. Taking into account the time derivative of the sub-scale velocity leads to improved numerical behavior that we have exploited for example in [30,32–34]. However, when the time step of the time discretization is not much smaller than $\rho\alpha_1$, this time derivative can be neglected, leading to what we call *quasi-static* sub-scales, which is the approach used in this work. In this case, problem (15)–(17) reduces to

$$\boldsymbol{u}'=\alpha_1 P'\left(\boldsymbol{R_u}\right),$$
$$p'=\alpha_2 P'\left(R_p\right),$$
$$\boldsymbol{\sigma}'=\alpha_3 P'\left(\boldsymbol{R_\sigma}\right).$$

All the approximations used heretofore will be used in our formulation. It remains only to define the space of sub-scales or, what is equivalent, the projection P'. As in previous works, two possibilities will be explored. In the first case, P' will be taken as the adequate identity I when applied to finite element residuals. We will refer to this approach as the ASGS (Algebraic Sub-Grid Scale) formulation. The sub-scales are then given by

$$\boldsymbol{u}'=\alpha_1\boldsymbol{R_u}, \tag{18}$$

$$p'=\alpha_2 R_p, \tag{19}$$

$$\boldsymbol{\sigma}'=\alpha_3\boldsymbol{R_\sigma}. \tag{20}$$

The second formulation that we will test, which we will refer to as OSS (Orthogonal Sub-scale Stabilization) method, considers that the space of sub-scales is orthogonal to the finite element space ($\boldsymbol{X}'=\boldsymbol{X}_h^{\perp}$), and then the expression of the sub-scales is

$$\boldsymbol{u}'=\alpha_1 P_h^{\perp}\left(\boldsymbol{R_u}\right)=\alpha_1\left(\boldsymbol{R_u}-P_h\left(\boldsymbol{R_u}\right)\right), \tag{21}$$

$$p'=\alpha_2 P_h^{\perp}\left(R_P\right)=\alpha_2\left(R_p-P_h\left(R_p\right)\right), \tag{22}$$

$$\boldsymbol{\sigma}'=\alpha_3 P_h^{\perp}\left(\boldsymbol{R_\sigma}\right)=\alpha_3\left(\boldsymbol{R_\sigma}-P_h\left(\boldsymbol{R_\sigma}\right)\right), \tag{23}$$

where P_h is the L^2 projection onto the appropriate finite element space.

A simple dimensional analysis reveals that the units of α_1 must be time divided by density (TL^3/M, if T is time, L is length and M is mass), whereas the units of α_2 and α_3 must be those of viscosity (M/LT). In this case, $\boldsymbol{u}'$ will be a velocity, p' a pressure and $\boldsymbol{\sigma}'$ a stress.

A discussion about the construction of the stabilizing parameter matrix for the Stokes problem can be found in [11]. In our case, we can follow a similar approach, now considering the existence of the convective term in the momentum equations and the fact that the viscosity is variable. The expression of matrix $\boldsymbol{\alpha}$ we will use is [23,35]:

$$\boldsymbol{\alpha}=\begin{bmatrix}\left[c_1\dfrac{\eta}{h_1^2}+c_2\dfrac{\rho\left|\boldsymbol{u}_h\right|}{h_2}\right]^{-1} & 0 & 0\\ 0 & c_3 2\eta & 0\\ 0 & 0 & c_4 2\eta\end{bmatrix}. \tag{24}$$

Here, η corresponds to the apparent viscosity of the fluid that in the Newtonian case is identical to the dynamic viscosity (μ), h_1 corresponds to a characteristic length calculated as the square root of the element area in the 2D case, and

as the cube root of the element volume in the 3D case, and h_2 corresponds to another characteristic length, calculated as the element length in the direction of the streamline. The constants $c_i, i = 1, 4$, are algorithmic parameters in the formulation. The values used in this work are $c_1 = 4.0, c_2 = 2.0$ and $c_3 = c_4 = 0.1$. In the case of higher order elements, the element lengths h_1 and h_2 in (24) are respectively divided by k^2 and k, k being the order of the finite element interpolation.

The two proposed stabilized formulations can be defined as residual-based. Consistency is ensured by construction. The stability constant depends on the value of the algorithmic constants $c_i, i = 1, 2, 3, 4$. The numerical analysis indicates that they have to be of order one (see [11]), and that $c_4 < 1$ (note that they are all dimensionless, and independent of the dimensionless numbers that govern the problem). The value $c_4 = 0.1$ has been found to give good results in the tests presented in this work, whereas $c_1 = 4.0, c_2 = 2.0$ are the optimal values for the approximation of the one-dimensional convection–diffusion equation.

We are now in a position to write the stabilized finite element formulations we will test. The abstract equation for the finite element component (12), which replaces the Galerkin finite element Eq. (4), now reads

$$\left(\rho\frac{\partial \boldsymbol{u}_h}{\partial t}, \boldsymbol{v}_h\right) + B(\boldsymbol{U}_h, \boldsymbol{V}_h) + \sum_K \left(\mathcal{L}^*\left(\boldsymbol{u}_h; \boldsymbol{V}_h\right), \boldsymbol{\alpha}\boldsymbol{R}_U\right)_K = \langle \boldsymbol{f}, \boldsymbol{v}_h\rangle \tag{25}$$

for the ASGS case, and:

$$\left(\rho\frac{\partial \boldsymbol{u}_h}{\partial t}, \boldsymbol{v}_h\right) + B(\boldsymbol{U}_h, \boldsymbol{V}_h) + \sum_K \left(\mathcal{L}^*\left(\boldsymbol{u}_h; \boldsymbol{V}_h\right), \boldsymbol{\alpha}\left(\boldsymbol{R}_U - P_h\left(\boldsymbol{R}_U\right)\right)\right)_K = \langle \boldsymbol{f}, \boldsymbol{v}_h\rangle, \tag{26}$$

in the case of orthogonal sub-scales (OSS), $\sum_K$ denoting summation for all elements of the finite element partition and $(\cdot,\cdot)_K$ the $L^2(K)$ inner product. In both formulations (25) and (26), the following term is added to the standard Galerkin formulation:

$$\begin{aligned}&\left(\mathcal{L}^*\left(\boldsymbol{a}; \boldsymbol{V}_h\right), \boldsymbol{\alpha}\boldsymbol{R}_U\right)_K \\ &= \int_K \begin{bmatrix} \nabla\cdot\boldsymbol{\tau}_h - \nabla q_h - \rho\boldsymbol{a}\cdot\nabla\boldsymbol{v}_h \\ -\nabla\cdot\boldsymbol{v}_h \\ \frac{1}{2\eta}\boldsymbol{\tau}_h + \nabla^s\boldsymbol{v}_h \end{bmatrix}^t \boldsymbol{\alpha} \begin{bmatrix} \boldsymbol{f} - \left(\rho\frac{\partial \boldsymbol{u}_h}{\partial t} - \nabla\cdot\boldsymbol{\sigma}_h + \rho\boldsymbol{a}\cdot\nabla\boldsymbol{u}_h + \nabla p_h\right) \\ -\nabla\cdot\boldsymbol{u}_h \\ -\frac{1}{2\eta}\boldsymbol{\sigma}_h + \nabla^s\boldsymbol{u}_h \end{bmatrix} \mathrm{d}K,\end{aligned} \tag{27}$$

with η computed with the velocity field $\boldsymbol{a}$. In the case of the OSS method, the contribution from the projection P_h in (26) needs also to be added.

The velocity field $\boldsymbol{a}$ appearing in (27) may be computed in several ways, depending on the linearization strategy and on whether the velocity sub-scales are taken into account or not in the advection velocity. If $\boldsymbol{a} = \boldsymbol{u}_h + \boldsymbol{u}'$, we call the sub-scales non-linear, in the sense that they are not neglected in the nonlinear terms. Even if this option has shown its superior performance, particularly in thermally coupled flows (see [36]) and can be shown to mimic the dissipative structure of the continuous problem (see [37]), we will approximate $\boldsymbol{a} \approx \boldsymbol{u}_h$. The iteration where this velocity is evaluated is indicated below.

Regarding the qualitative comparison between (25) and (26), it has to be noted that both formulations are consistent, and that the latter introduces less dissipation, in the sense that only the component of (part of) the finite element residual orthogonal to the finite element space appears as dissipation when the test function is taken equal to the finite element unknown.

3.4. Fully discrete and linearized problem

The Navier–Stokes problem to be solved has two sources of nonlinearity, namely, the convective term and the constitutive law. When the equations are discretized using the finite element method described, other nonlinearities appear because of the dependence of the stabilizing terms on the velocity.

For the sake of conciseness, we will consider only a fixed-point iterative scheme and the second order BDF scheme for the time integration, since this linearization is stable for divergence free velocities (another possibility would be to use a Newton–Raphson scheme or variants of it). In particular, the stabilization parameters in (24) are assumed to

be computed with a given velocity guess and iteratively updated, also neglecting the velocity sub-scale. If we denote with a double superscript the time step and iteration counter, the problem to be solved at time step $j+1$ to find the $i+1$ iterate of the unknowns is given by:

$$\left(\rho\frac{3\boldsymbol{u}_h^{j+1,i+1}}{2\delta t},\boldsymbol{v}_h\right)+\left(\nabla^s\boldsymbol{v}_h,\boldsymbol{\sigma}_h^{j+1,i+1}\right)+\left(\rho\boldsymbol{u}_h^{j+1,i}\cdot\nabla\boldsymbol{u}_h^{j+1,i+1},\boldsymbol{v}_h\right)-\left(p_h^{j+1,i+1},\nabla\cdot\boldsymbol{v}_h\right)$$
$$+\sum_K\left(-\rho\boldsymbol{u}_h^{j+1,i}\cdot\nabla\boldsymbol{v}_h,\alpha_1P'(\boldsymbol{R_u})\right)_K+\sum_K\left(-\nabla\cdot\boldsymbol{v}_h,\alpha_2P'\left(R_p\right)\right)_K+\sum_K\left(\nabla^s\boldsymbol{v}_h,\alpha_3P'(\boldsymbol{R_\sigma})\right)_K$$
$$=\langle\boldsymbol{f},\boldsymbol{v}_h\rangle+\left(\rho\frac{4\boldsymbol{u}_h^{j}-\boldsymbol{u}_h^{j-1}}{2\delta t},\boldsymbol{v}_h\right),\tag{28}$$

$$\left(q_h,\nabla\cdot\boldsymbol{u}_h^{j+1,i+1}\right)+\sum_K\left(-\nabla q_h,\alpha_1P'(\boldsymbol{R_u})\right)=0,\tag{29}$$

$$\left(\frac{1}{2\eta^{j+1,i}}\boldsymbol{\sigma}_h^{j+1,i+1},\boldsymbol{\tau}_h\right)-\left(\nabla^s\boldsymbol{u}_h^{j+1,i+1},\boldsymbol{\tau}_h\right)$$
$$+\sum_K\left(\nabla\cdot\boldsymbol{\tau}_h,\alpha_1P'(\boldsymbol{R_u})\right)_K+\sum_K\left(\frac{1}{2\eta^{j+1,i}}\boldsymbol{\tau}_h,\alpha_3P'(\boldsymbol{R_\sigma})\right)_K=0,\tag{30}$$

for all $[\boldsymbol{v}_h,q_h,\boldsymbol{\tau}_h]\in\boldsymbol{X}_h$, where converged values at a given time step have only the time step superscript and P' is the identity in the ASGS formulation and $P_h^{\perp}$ in the OSS method.

Algorithm 1 describes the flow of calculations to solve the problem. The possibility of using under-relaxation is taken into account through the parameter β, with $0<\beta\leq1$.

Algorithm 1 Stabilized formulations: ASGS and OSS

READ $\boldsymbol{u}_h^0$ (initial condition)
SET $p_h^0=0,\boldsymbol{\sigma}_h^0=0$
FOR, $j=0,\ldots,N-1$ DO (temporal loop, N number of time steps):
  SET $i=0$
  SET $\boldsymbol{u}_h^{j+1,0}=\boldsymbol{u}_h^j$, $p_h^{j+1,0}=p_h^j$ and $\boldsymbol{\sigma}_h^{j+1,0}=\boldsymbol{\sigma}_h^j$
  WHILE not converged DO:
    $i\leftarrow i+1$
    SET$\boldsymbol{a}^{j+1,i}=\boldsymbol{u}_h^{j+1,i-1}$
    COMPUTE $\eta^{j+1,i}$ (from the constitutive equation)
    IF(OSS case)
      COMPUTE $P_h(\boldsymbol{R}_{\boldsymbol{U}}^{j+1,i})$
    END IF
    COMPUTE α_1,α_2 and α_3 (stabilization parameters) from (24)
    SOLVE FOR $\boldsymbol{u}_h^{j+1,i}$, $p_h^{j+1,i}$ and $\boldsymbol{\sigma}_h^{j+1,i}$ from (28)–(30)
    $\boldsymbol{u}_h^{j+1,i}\leftarrow\beta\boldsymbol{u}_h^{j+1,i}+(1-\beta)\,\boldsymbol{u}_h^{j+1,i-1}$
    $p_h^{j+1,i}\leftarrow\beta p_h^{j+1,i}+(1-\beta)\,p_h^{j+1,i-1}$
    $\boldsymbol{\sigma}_h^{j+1,i}\leftarrow\beta\boldsymbol{\sigma}_h^{j+1,i}+(1-\beta)\,\boldsymbol{\sigma}_h^{j+1,i-1}$
    CHECK convergence
  END WHILE
  SET converged values
  $\boldsymbol{u}_h^{j+1}=\boldsymbol{u}_h^{j+1,i}$
  $p_h^{j+1}=p_h^{j+1,i}$
  $\boldsymbol{\sigma}_h^{j+1}=\boldsymbol{\sigma}_h^{j+1,i}$
END DO (temporal loop)

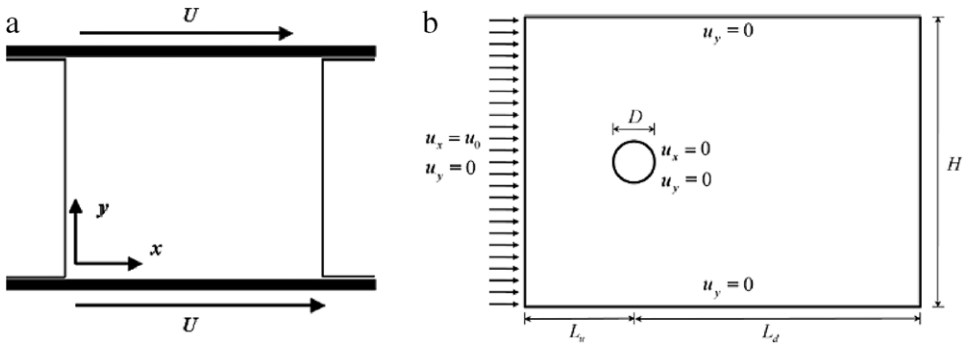

Fig. 1. Schematic representation of the problems analyzed: (a) mixing cavity and (b) flow over a cylinder.

4. Numerical results

This section shows the different test cases used to evaluate the performance of the stabilized formulations proposed in this work, both in the cases of non-linear viscosity and of dominant convection, in steady-state and in transient problems.

We will first present a convergence test (in Section 4.1) and then move to two 2D examples. Fig. 1 schematizes the problems considered in this case, namely, (a) the parallel flow mixing cavity and (b) the flow over a cylinder, discussed in Sections 4.2 and 4.3, respectively. The spatial discretization can be seen in Fig. 2. A structured triangular mesh of 12,961 nodes and 25,600 linear elements will be used in the mixing cavity problem (Fig. 2(a)) for all cases, whereas a triangular mesh of 43,183 nodes and 82,588 linear elements will be used for the flow over a cylinder. A zoom of this mesh is shown in Fig. 2(b). This section will conclude with the evaluation of the formulation to compute shear stresses on walls using two 3D examples (Section 4.4).

The discrete linearized problem is solved in all cases by using an iterative solver based on the Generalized Minimal Residual Method (GMRES) of Saad and Schultz [38], with an incomplete-LU (ILU) factorization as a preconditioner.

4.1. Convergence test

The first set of results shown corresponds to the convergence analysis of the stabilized formulations used in the three-field Navier–Stokes problem with non-linear viscosity, where the fluid is characterized by a quasi-Newtonian Ostwald–de Waele model. The range of the power-law indexes is $0.5 \leq n \leq 1.5$ and the range of Reynolds numbers $0.3 \leq \mathrm{Re} \leq 400$. A force term is introduced in the momentum equation so that the exact solution is given by

$$
\begin{aligned}
u(x, y) &= 2x^2 y\,(x-1)^2\,(y-1)^2\,(2y-1)\,,\\
v(x, y) &= 2xy^2\,(x-1)^2\,(y-1)^2\,(2x-1)\,,\\
p(x, y) &= \sin(2\pi x)\sin(2\pi y)\,,
\end{aligned}
$$

$u(x, y)$ and $v(x, y)$ being the x- and y-velocity components, respectively.

The stress field is derived from the constitutive equation that relates the stress tensor with the symmetrical velocity gradient, including therefore the non-Newtonian effect of the viscosity. The stresses in this 2D case are explicitly given by

$$
\sigma_{xx}(x, y) = 2\eta\frac{\partial u_x}{\partial x}, \qquad \sigma_{yy}(x, y) = 2\eta\frac{\partial u_y}{\partial y}, \qquad \sigma_{xy}(x, y) = \eta\left(\frac{\partial u_x}{\partial y} + \frac{\partial u_y}{\partial x}\right).
$$

The computational domain is the unit square, discretized using uniform structured meshes of linear and quadratic triangular elements, the range of element sizes being $0.005 \leq h \leq 0.1$. From the physical point of view, the complexity of the test relies on the non-linearity of the viscosity modeled as a power law. In Fig. 3 one can see the viscosity field for pseudo-plastic and dilatant fluids, respectively. It is worth noting that in both cases there are singularities in the viscosity field, both at the four corners and at the center point of the domain. In the dilatant fluid ($n = 1.5$), the minimum viscosity value is zero, while in the pseudo-plastic case ($n = 0.5$), the maximum viscosity value tends to infinity.

The maximum viscosity values obtained at the numerical integration points for the two numerical formulations studied are detailed in Table 1. It can be noted that in both fluids the OSS method captures better the limit values of

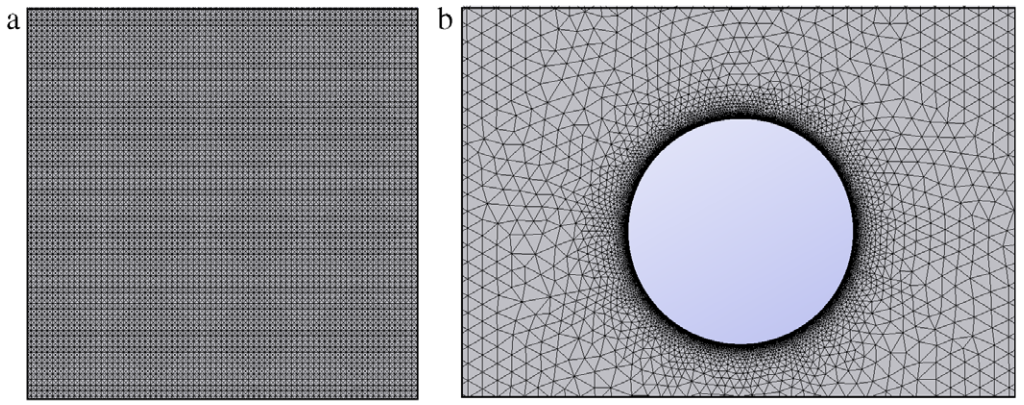

Fig. 2. Mesh used in problems: mixing cavity (a) and flow over a cylinder (b).

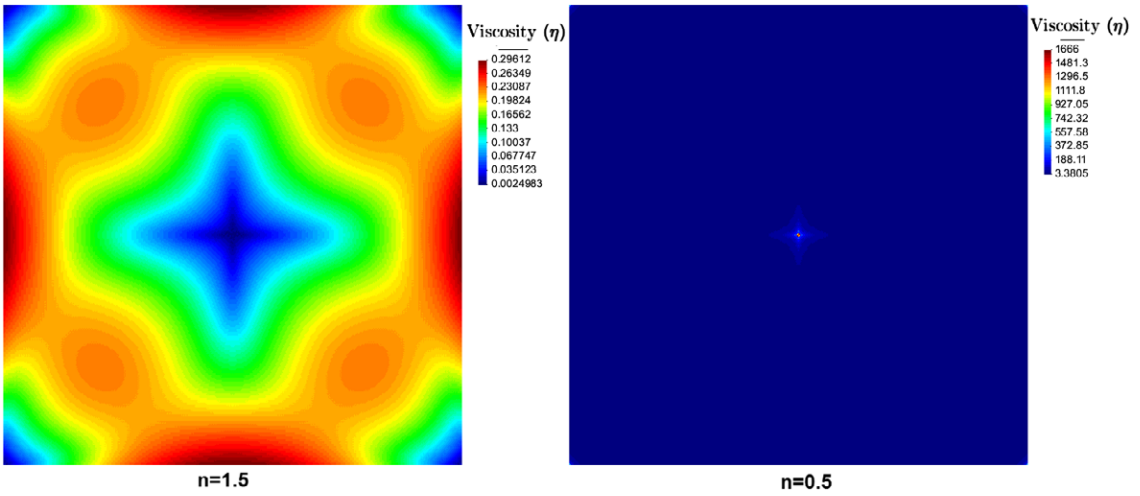

Fig. 3. Contours of viscosity obtained in the convergence test problem in dilatant fluid ($n = 1.5$) and pseudo-plastic fluid ($n = 0.5$). (For interpretation of the references to color in this figure legend, the reader is referred to the web version of this article.)

Table 1
Viscosity limit values obtained in the convergence test problem, in pseudoplastic fluid ($n = 0.5$) and dilatant fluid ($n = 1.5$), using the stabilized formulations ASGS and OSS.

$n = 0.5$	ASGS	OSS	Dif(OSS–ASGS)
η_{max}	1498.7	1666	10.04%
η_{min}	3.4169	3.3805	1.07%
$n = 1.5$	ASGS	OSS	Dif(OSS–ASGS)
η_{max}	0.29569	0.29612	0.145%
η_{min}	0.0030626	0.00249	22.99%

viscosity, both the maximum and the minimum values. In the pseudo-plastic case we obtain a difference between the OSS and the ASGS formulations (Dif(OSS–ASGS)) equal to 10.04% and in the dilatant case a difference equal to 22.99%, in both cases using the OSS estimation as a reference value (see Table 1).

The optimal convergence rate expected when the mesh size is reduced using linear triangular elements is two in velocity and one in pressure and stress in the L^2-norm, while using quadratic triangular elements it is three in velocity and two in pressure and stress. The graphs in Figs. 4 and 5 show the obtained results using the ASGS formulation and the OSS method in the three-field problem, also compared with the analogue in the two-field case using the ASGS

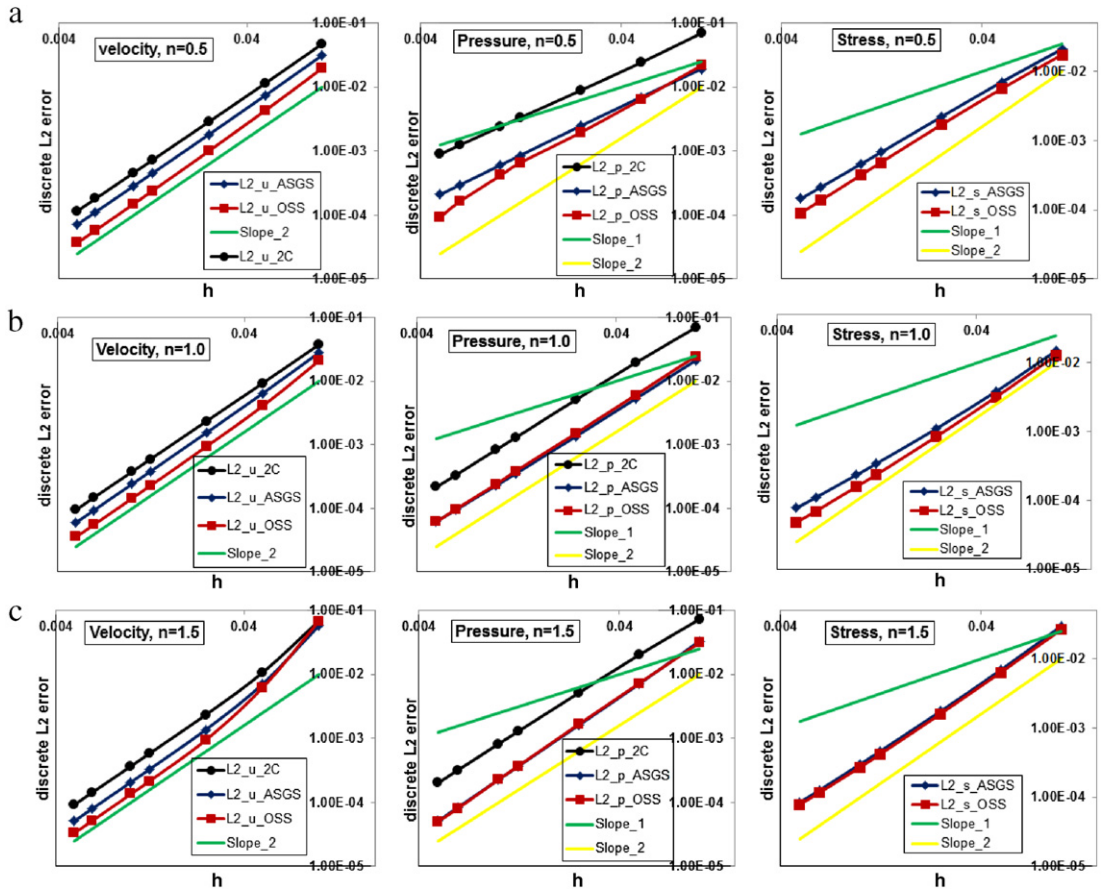

Fig. 4. Convergence of the velocity–pressure–stress fields, in linear triangular elements for the different power-law indexes analyzed: (a) $n = 0.5$, (b) $n = 1$ y and (c) $n = 1.5$.

formulation [29]. Regarding the nomenclature used in the graphs, L2_U_2C corresponds to the L^2-norm in the two-field case, while L2_U_ASGS and L2_U_OSS, corresponds to the ASGS and OSS cases in the proposed three-field formulation, where U is the variable whose convergence is evaluated. The reference lines, Slope_(1, 2 and 3), allow one to evaluate the behavior of the schemes, where 1–3 are the values of the slope in each of them.

We remark that the two-field approach follows simply changing the space of stresses so that $\boldsymbol{\sigma}_h = 2\eta\nabla^s\boldsymbol{u}_h$, with the viscosity evaluated at the integration points, and setting $\alpha_3 = 0$ (no stress stabilization is required). The rest of parameters of both formulations are the same. Likewise, in the numerical examples we have used the same convergence tolerance in the discrete L^2 norm of velocities.

Independently of the power index employed, both stabilized formulations of three fields show better accuracy properties than their counterpart in two fields, yielding in all cases optimal slopes in the convergence curves. It is also worth noting that the OSS method generates a smaller error for all the cases analyzed, both in velocity and stress, and it behaves almost like the ASGS formulation in pressure. For quadratic elements (Fig. 5) only the ASGS case is shown. Optimal convergence rates are found for all variables.

The expected convergence orders are those of the interpolation error in the adequate norm. This is the best one can expect and what is proved in [11]. However, for smooth solutions as the one considered in our convergence test, a super-convergent behavior can be observed, and this is what happens in for the pressure and the stress using linear elements. For quadratic elements, the asymptotic convergence rate is the theoretical one. Note that the convergence analysis is intended to be valid *in all situations*, and thus it does not seem possible to expect more than convergence of order k (interpolation order) for pressure and stresses.

The non-Newtonian effect can be appreciated in the stress field. Fig. 6 shows the σ_{xx} component for the three fluids analyzed.

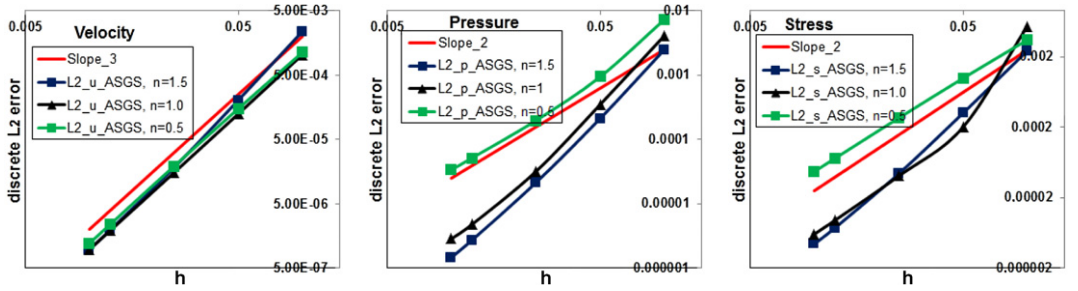

Fig. 5. Convergence of the velocity–pressure–stress fields, in quadratic triangular elements for the different power-law indexes analyzed.

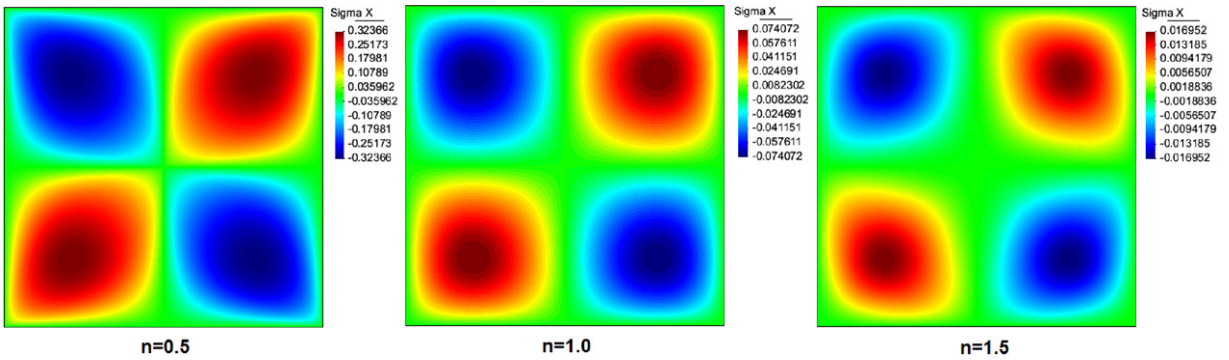

Fig. 6. Contours of the normal stress component σ_{xx}, obtained in the convergence test problem for the different power-law fluids analyzed. (For interpretation of the references to color in this figure legend, the reader is referred to the web version of this article.)

4.2. *Parallel lid-driven cavity problem in non-linear viscosity fluids*

The problem of the mixing cavity is a recurrent test in the approximation of non-Newtonian fluid flows. The results shown below correspond specifically to a unit square, subjected to a unidirectional velocity field in the parallel horizontal faces and zero velocity in the vertical faces (Fig. 1(a)). The results obtained are compared with those published by Mendu and Das [24] for a power-law fluid. In addition, a more convective case than those in the cited reference is also considered, using now Carreau–Yasuda models of shear-thinning and shear-thickening types.

It is important to define the power-law Reynolds number:

$$\mathrm{Re}_{\mathrm{PL}} = \frac{\rho U^{2-n} L_c^n}{m},$$

where ρ is the fluid density, U the mixing velocity (see Fig. 1(a)), L_c a characteristic length ($L_c = 1$ in this problem), n the power-law index and m the consistency index in the power-law. The Newtonian case is reproduced when $n = 1$ and $m = \mu$, obtaining the standard expression of the Reynolds number Re. In the Carreau–Yasuda fluid, the Reynolds number is calculated in the standard manner, using the minimum value of the viscosity ($\eta_{\min}$), that is, $\mathrm{Re} = \frac{\rho U L_c}{\eta_{\min}}$.

Before comparing the results obtained with our formulations, we present in Table 2 the results of a mesh refinement study conducted to select the working mesh. For different values of exponent n, we show the location of the upper vortex for the higher Reynolds number obtained using three different meshes with increasing number of elements. It is observed from Table 2 that the differences observed when using meshes M2 and M3 are negligible, and results agree with those presented in [24]. We have used mesh M2 in all the results to be described next.

Table 3 shows and compares the results obtained with those published in [24]. It is noteworthy that in [24] the lattice Boltzmann scheme was used for the calculation, employing a mesh of 257 × 257 points, while in the present work the structured mesh used was composed of 12,961 linear triangular elements (Fig. 2(a)). In the two proposed formulations the location of the primary vortex is identical.

The results published by Mendu and Das [24] comprise the range of Reynolds numbers $100 \leq \mathrm{Re}_{\mathrm{PL}} \leq 1000$. As an additional test, we considered a more convective problem ($\mathrm{Re}_{\mathrm{PL}} = 5000$) to show the stabilizing properties of the two presented formulations.

Table 2
Mesh refinement study in the parallel lid-driven cavity problem for different power law indexes in the location of the upper vortex (x-coordinate/y-coordinate). The number of nodes/number of elements is indicated below each mesh label.

$Re_{PL} = 1000$	Mesh M1	Mesh M2	Mesh M3
n	3281/6400	12,961/25,600	20,201/40,000
$n = 0.5$	0.5125/0.75	0.5625/0.75	0.56/0.75
$n = 1.0$	0.55/0.75	0.5375/0.75	0.54/0.75
$n = 1.5$	0.55/0.75	0.54375/0.75625	0.545/0.755

Table 3
Location of primary vortex mixing cavity problem for the different power indexes analyzed (Ref. [24]/present work): (a) $n = 1.0$, (b) $n = 0.5$ and (c) $n = 1.5$.

Re_{PL}	x_coord	y_coord	dif_x	dif_y	x_coord	y_coord	dif_x	dif_y
(a)	Upper	($n = 1.0$)			Lower	($n = 1.0$)		
100	0.6187/0.6131	0.7937/0.7964	0.92%	0.33%	0.6187/0.6131	0.2062/0.2059	0.92%	0.17%
400	0.5937/0.5863	0.7562/0.7607	1.27%	0.58%	0.5937/0.5863	0.2437/0.2396	1.27%	1.73%
1000	0.5375/0.5364	0.75/0.7544	0.21%	0.58%	0.5375/0.5364	0.25/0.248	0.21%	0.81%
5000	0.5125	0.75	–	–	0.5125	0.25	–	–
(b)	Upper	($n = 0.5$)			Lower	($n = 0.5$)		
100	0.7187/0.7186	0.8250/0.8196	0.02%	0.66%	0.7187/0.7186	0.1812/0.1807	0.02%	0.30%
400	0.65/0.6419	0.75/0.7523	1.26%	0.31%	0.65/0.6419	0.25/0.2459	1.26%	1.67%
1000	0.5625/0.5732	0.75/0.7503	1.87%	0.04%	0.5625/0.5732	0.25/0.2522	1.87%	0.87%
5000	0.55625	0.74375	–	–	0.55625	0.25625	–	–
(c)	Upper	($n = 1.5$)			Lower	($n = 1.5$)		
100	0.5437/0.5499	0.7812/0.7859	1.12%	0.59%	0.5437/0.5499	0.2187/0.2164	1.12%	1.09%
400	0.5812/0.5805	0.7687/0.7691	0.13%	0.05%	0.5812/0.5805	0.2312/0.2312	0.13%	0.02%
1000	0.5437/0.5422	0.7562/0.7586	0.29%	0.31%	0.5437/0.5422	0.2437/0.2438	0.29%	0.02%
5000	0.5125	0.75	–	–	0.5125	0.25	–	–

Table 4
Constants of the Carreau–Yasuda model in the mixing cavity problem (SI units).

Fluid type	μ_0	μ_∞	λ	n	a	ρ
Shear-thinning	0.056	0.00345	1.902	0.22	1.25	1
Shear-thickening	0.00345	0.056	1.902	0.22	1.25	1

The excellent correlation of our results with those published in [24] can be observed from Table 3. The maximum difference in coordinates in the location of the primary vortexes is 1.87% for a fixed mesh five times coarser than that used in [24], independently of the power-law index and the Reynolds number considered, thus showing the robustness of both VMS schemes proposed, in dominant convection and in the case of nonlinear viscosity.

For the Carreau–Yasuda fluid, the constants that define if the fluid is shear-thinning or shear-thickening are presented in Table 4.

The results of primary vortexes location and number of iterations for each of the formulations are shown in Table 5 for the Carreau–Yasuda fluid. The minimum and maximum viscosity and pressure values obtained are also indicated. The location of vortexes is identical in both formulations, and only results for the OSS method are shown. Viscosity peaks differ slightly and are given for both the ASGS and the OSS formulations.

Regarding the results presented in Table 5, it can be observed that always a greater pressure difference between pressure peaks is found in the OSS formulation, although the location of primary vortexes is the same in the two formulations. The viscosity peaks are practically identical and are bounded by the limit values indicated in Table 4, thus regulating the behavior of the model independently of the value of the second invariant of the strain rate tensor

Table 5
Location of primary vortexes, number of iterations and peaks of viscosity–pressure in Carreau–Yasuda fluids, for the ASGS and the OSS formulations.

Upper	x_coord	y_coord	**Viscosity peaks**	$\eta_{\min}$	$\eta_{\max}$
Shear-thinning	0.5125	0.75	Shear-thinning ASGS	0.0034506	0.05862
Shear-thickening	0.6125	0.7625	Shear-thinning OSS	0.0034506	0.05434
Lower	x_coord	y_coord	Shear-thickening ASGS	0.009115	0.055999
Shear-thinning	0.5125	0.25	Shear-thickening OSS	0.00919	0.05599
Shear-thickening	0.6125	0.2375	**Pressure peaks**	$p_{\min}$	$p_{\max}$
Number of iterations	ASGS	OSS	Shear-thinning ASGS	−38.715	98.497
Shear-thinning	141	138	Shear-thinning OSS	−38.806	100.29
Shear-thickening	53	53	Shear-thickening ASGS	−40.722	385.6
			Shear-thickening OSS	−41.657	386.73

Table 6
Iterations required for convergence in the mixing cavity problem with a power-law fluid for the two proposed stabilized formulations.

Power-law index	$n = 0.5$	$n = 1.0$	$n = 1.5$
Iterations	ASGS/OSS	ASGS/OSS	ASGS/OSS
$\mathrm{Re}_{\mathrm{PL}} = 100$	35/37	17/17	23/24
$\mathrm{Re}_{\mathrm{PL}} = 400$	83/90	38/38	47/47
$\mathrm{Re}_{\mathrm{PL}} = 1000$	94/113	45/44	58/58
$\mathrm{Re}_{\mathrm{PL}} = 5000$	131/141	104/130	62/82

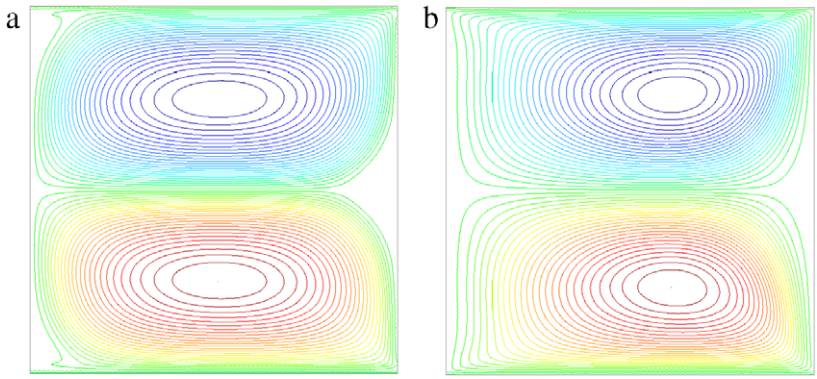

Fig. 7. Streamlines in Carreau–Yasuda fluids: (a) Shear-thinning, (b) Shear-thickening.

in the constitutive model. This eliminates any singularity in the viscosity field, as it occurs with the power-law model. Fig. 7 show the streamlines for the Carreau–Yasuda fluids in the two cases considered.

Since the projection of the residual in the OSS method is evaluated in the previous iteration, it is important to compare the number of iterations required to reach convergence for the ASGS and the OSS formulations. Table 6 indicates this number of iterations necessary to achieve a convergence error smaller than 10^{-8} in the discrete L^2 norm of the unknowns. In general it can be observed that a slightly higher number of iterations is required in the OSS formulation. This however may be compensated by a higher accuracy, as observed in the convergence test and in the better reproduction of peaks of the unknowns using the OSS method.

From the physical standpoint, the flow presents pressure peaks at the corners of the computational domain. Fig. 8 shows the pressure isolines for the case $\mathrm{Re} = 5000$ in the case of a Newtonian fluid, where it can be seen that the pressure peaks are greater in the OSS formulation. Similar results were presented in Table 5 for the Carreau–Yasuda fluid, in addition to the maximum and minimum values of the viscosity (Table 1) obtained in the previous sub-section. As it can be observed, the capability to represent in a better manner the singular points by the OSS formulation is a general tendency.

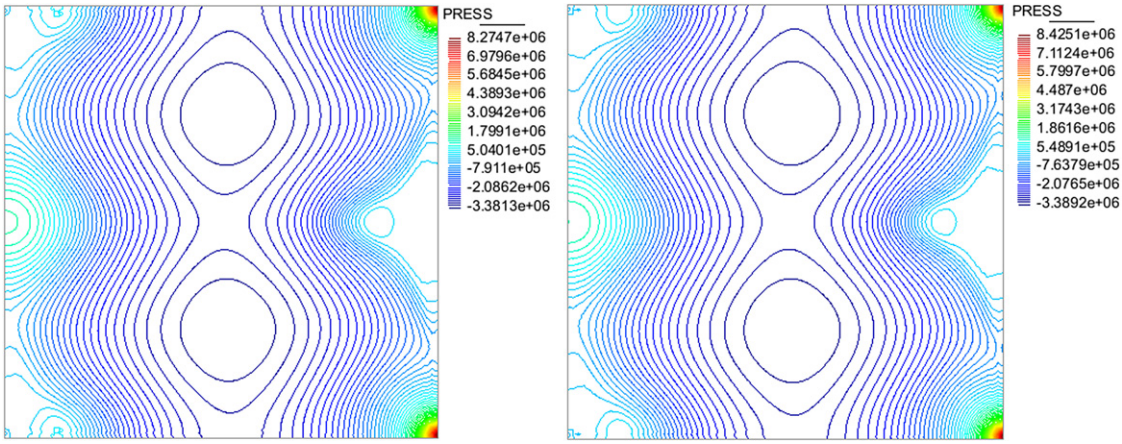

Fig. 8. Pressure isolines in Newtonian fluid (Re = 5000), left: ASGS formulation; right: OSS formulation. (For interpretation of the references to color in this figure legend, the reader is referred to the web version of this article.)

4.3. Transient flow of a power-law fluid over a cylinder

The problem of flow over a cylinder has been studied by a great number of authors over the years, both in the stationary case and in the transient regime. The fluid dynamics that develops when the flow collides with the solid cylinder varies considerably with the Reynolds number, going from a steady state to a periodically time varying state, presenting in the latter case the characteristic von Karman vortexes. The critical Reynolds number that determines the beginning of the oscillatory behavior lies in the range $40 \leq \mathrm{Re} \leq 50$ in Newtonian fluids.

In the case of non-linear viscosity, results are more scarce, especially at high Reynolds numbers, where the dominant convection is combined with the non-linearity of the viscosity. Patnana et al. analyzed in [25] the problem of the flow of a power-law fluid over a cylinder in the range of Reynolds numbers $40 \leq \mathrm{Re}_{\mathrm{PL}} \leq 140$ with a commercial software. They found different correlations between macroscopic parameters, as the coefficients of drag–lift and the Strouhal number, with the power-law index that characterizes the fluid for a fixed Reynolds number.

When a transient problem is analyzed, an important parameter that defines the dimensionless frequency of the fluid dynamics is the Strouhal number, which is defined as

$$\mathrm{St} = \frac{f D}{u_0},$$

where f corresponds to the oscillatory frequency of the problem, D represents the diameter of the cylinder and u_0 is a characteristic velocity, which in the present case corresponds to the inlet velocity u_0 (Fig. 1(b)).

Let F_{D} and F_{L} be the drag and lift forces, respectively. The dimensionless drag and lift coefficients are computed as

$$\mathrm{C_D} = \frac{F_{\mathrm{D}}}{(1/2)\rho u_0^2 D}, \qquad \mathrm{C_L} = \frac{F_{\mathrm{L}}}{(1/2)\rho u_0^2 D}.$$

If we increase the size of the computational domain, the boundary conditions are less influential on the velocity, pressure and stress fields, but of course at a higher computational cost. Patnana et al. [25], studied the influence of the dimensions of the domain around the cylinder in the macroscopic parameters, without encountering important variations in the value of the drag–lift coefficients and in the Strouhal number for domains larger than the one we have chosen. It is a rectangle of dimensions $[0, 16] \times [0, 8]$, with a cylinder of unitary diameter centered at point (4, 4). The mesh used in this problem consists of 82,588 linear triangular elements and 43,183 nodes, mostly concentrated in the area close to the cylinder (Fig. 2(b)). Regarding the boundary conditions applied to the problem, the inlet condition (at $x = 0$) corresponds to a constant velocity field with components $\boldsymbol{u} = (u_0, 0)$, the boundaries $y = 0,\ y = 8$ are left free in the horizontal component and the vertical velocity is prescribed to zero, while on the outlet ($x = 16$) both velocity components are left free.

From the physical standpoint, the lift coefficient C_{L} oscillates between two extreme values with zero mean because of symmetry. The first order backward Euler scheme is able to capture the oscillation frequency (St), but yields a poor

Table 7
Mesh dependency study for $C_{\overline{D}}$ (mean drag coefficient), $C_{L,max}$ (maximum lift coefficient), and St for the flow over a cylinder problem using different power law indexes and $Re_{PL} = 140$. Mesh M1 (31,710 nodes, 61,211 elements) and mesh M2 (43,182 nodes, 82,588 elements).

n	δt_1	δt_2	M1, δt_1			M2, δt_1			M2, δt_2		
			$C_{\overline{D}}$	$C_{L,max}$	St	$C_{\overline{D}}$	$C_{L,max}$	St	$C_{\overline{D}}$	$C_{L,max}$	St
0.4	0.005	0.0025	1.2646	0.8147	0.2278	1.2684	0.8182	0.2278	1.2667	0.855	0.2300
0.6	0.005	0.0025	1.2922	0.6337	0.2171	1.2937	0.6340	0.2142	1.2960	0.6342	0.2142
1.0	0.001	0.0005	1.4272	0.5013	0.1930	1.4270	0.5015	0.1925	1.4250	0.5005	0.1920
1.4	0.001	0.0005	1.6232	0.4469	0.1801	1.6235	0.4481	0.1805	1.6230	0.4480	0.1800
1.8	0.001	0.0005	1.7795	0.4253	0.1660	1.7700	0.4250	0.1655	1.7701	0.4205	0.1650

Table 8
Comparison of macroscopic parameters in the flow over a cylinder problem. $C_{\bar{D}}$: mean drag coefficient, $C_{L,max}$: maximum lift coefficient in time.

Source	$C_{\bar{D}}$	Source	$C_{\bar{D}}$	$C_{L,max}$	St
Re = 40, $n = 0.6$		Re = 140, $n = 0.4$			
Present study	1.4316	Present study	1.2667	0.855	0.2300
Patnana et al. [25]	1.3576	Patnana et al. [25]	1.2514	0.9983	0.2262
Bharti et al. [39]	1.3717	Re = 140, $n = 0.6$			
Soares et al. [40]	1.3900	Present study	1.2960	0.6342	0.2142
Re = 40, $n = 1.4$		Patnana et al. [25]	1.2560	0.7453	0.2128
Present study	1.6792	Re = 140, $n = 1.0$			
Patnana et al. [25]	1.6541	Present study	1.4250	0.5005	0.1920
Bharti et al. [39]	1.6429	Patnana et al. [25]	1.3579	0.4936	0.1851
Soares et al. [40]	1.6200	Re = 140, $n = 1.4$			
Re = 40, $n = 1.8$		Present study	1.6230	0.4480	0.1800
Present study	1.9437	Patnana et al. [25]	1.49369	0.4072	0.1721
Patnana et al. [25]	1.8726	Re = 140, $n = 1.8$			
Bharti et al. [39]	1.9556	Present study	1.7701	0.4235	0.1650
		Patnana et al. [25]	1.6265	0.3436	0.1529

approximation to the maximum values of C_L. On the other hand, the second order BDF2 scheme yields a much better approximation to the amplitude of C_L. The results shown below were calculated using this second order scheme.

We present in Table 7 the values computed of different coefficients for two meshes and different time step sizes. In fact, we have computed these coefficients with more time step sizes. The results presented are only intended to show how they are influenced by mesh refinement. Even if the difference is not very important, the results presented next have been obtained using the small time step size δt_2 (which varies according to power n) and the refined mesh M2.

Table 8 has the purpose of validating the results in the transient problem for the power-law fluid. Since transient non-Newtonian results are scarce, it also includes a stationary sub-case for a Reynolds number $Re_{PL} = 40$, with the purpose of comparing the results with other authors [39,40].

As shown in Table 8, results are in a reasonable agreement between the different sources. The most important differences occur for high values of the power-law index. Let us remark that the transient values published by Patnana et al. in [25] were obtained with the Finite Volume Method, using a second order upwind scheme for the convective term, the SIMPLE algorithm and a second order time integration scheme with a mesh with 212,323 cells, three times more than in the mesh used in the present work.

In general, for a fixed Reynolds number the drag coefficient is increased when the power-law index is increased. The opposite happens with the lift coefficient and the Strouhal number. Fig. 9 shows the correlation between these parameters for the case $Re_{PL} = 140$. This agrees with the tendency shown in [25]. The normalization of results in Fig. 9 is performed by dividing the value obtained for the specific variable computed with the power index that defines the problem, say $g(n)$, by the value of the same variable in the Newtonian case, that is to say, $g(n = 1)$, where function $g(\cdot)$ corresponds to the Strouhal number or the drag–lift coefficients, depending on the case.

Let us show now some results obtained with the proposed three-field stabilized formulations for the pseudo-plastic fluid ($n = 0.4$) and for the dilatant fluid ($n = 1.8$). It is noteworthy that both in the ASGS and in the OSS formulations

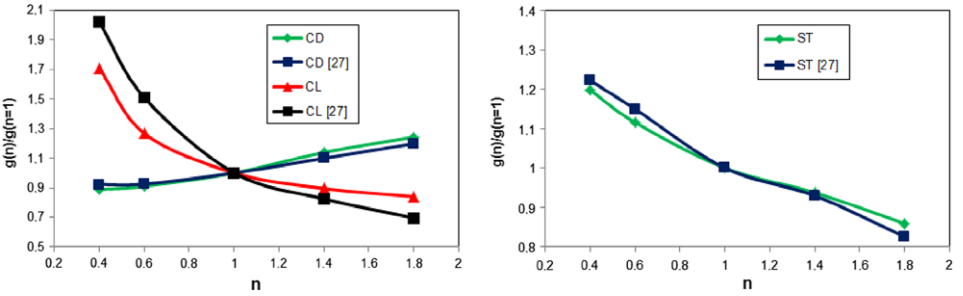

Fig. 9. Influence of the power-law index (n), in the drag coefficient (C_D), the lift coefficient (C_L) and the Strouhal number (St).

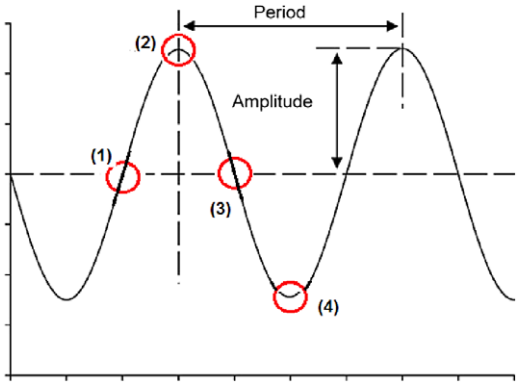

Fig. 10. Wave scheme to define some comparison points.

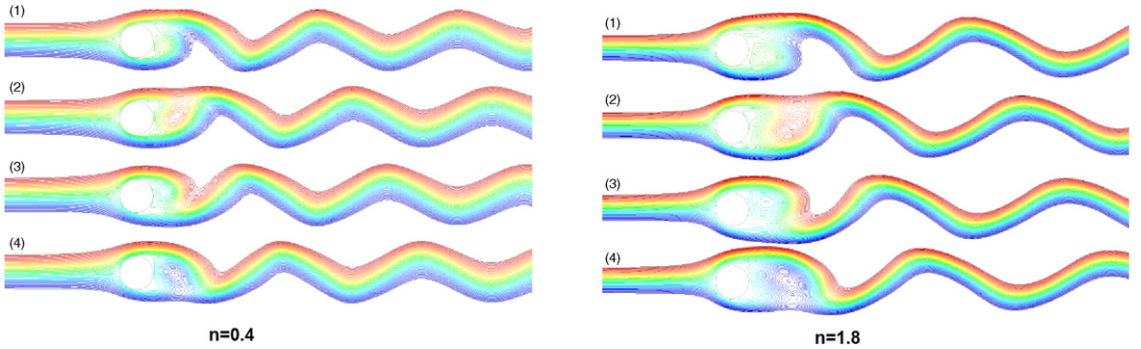

Fig. 11. Evolution of the streamlines close to the cylinder, from the input condition to the output condition in the problem of flow over a cylinder in pseudoplastic ($n = 0.4$) and dilatant ($n = 1.8$) fluids.

these results are very similar, so that the contours and the isolines of some of the variables are displayed without indicating the formulation employed.

In order to compare the physical behavior of pseudo-plastic and dilatant fluids, we plot in Fig. 11 the streamlines corresponding to the solution obtained using $n = 0.4$ (pseudo-plastic case) and $n = 1.8$ (dilatant case). The time instants correspond to positions (1)–(4) in Fig. 10.

From Fig. 11 it can be observed that the recirculation zone is bigger in the case of a dilatant fluid. This gives rise to a higher period of oscillations, that is to say, the oscillation frequency is higher for pseudo-plastic fluids. This agrees with the Strouhal numbers obtained in each case.

The contour plots of the stress component σ_{xx} are depicted in Fig. 12 in the case of a pseudo-plastic fluid. Once again, the snapshots correspond to the time instants indicated in Fig. 10.

Finally, Fig. 13 illustrates the nonlinearity and dynamic behavior in the viscosity field for $\mathrm{Re}_{\mathrm{PL}} = 140$ and $n = 1.8$. Note that the consistency index used for the dilatant case $n = 1.8$ is $m = 0.02$, with a maximum value for the viscosity

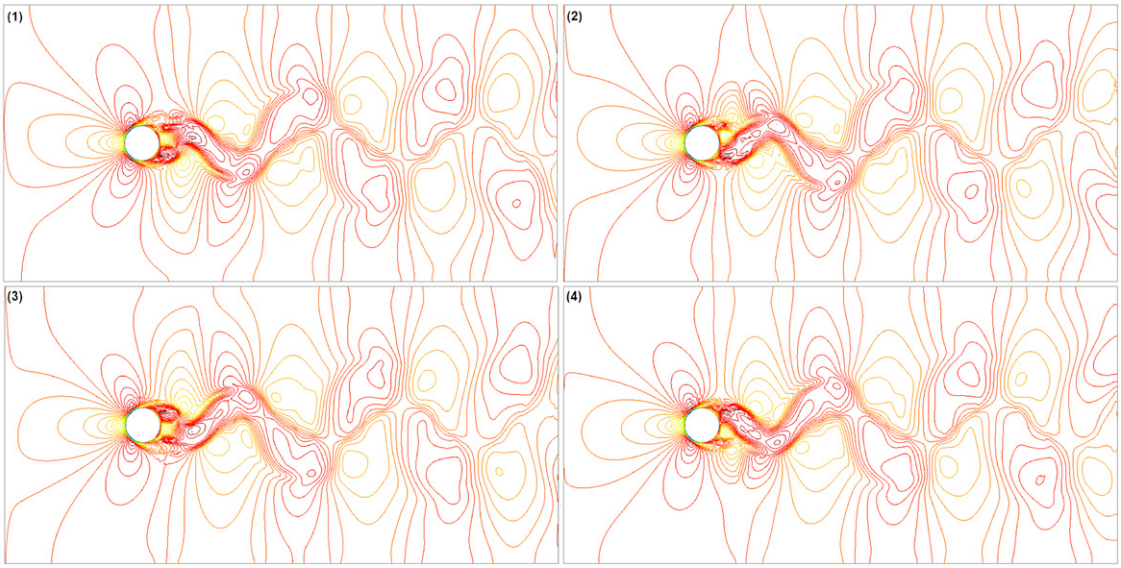

Fig. 12. Contours of stress σ_{xx} in the cylinder problem for the case $n = 0.4$ and $\mathrm{Re}_{\mathrm{PL}} = 140$.

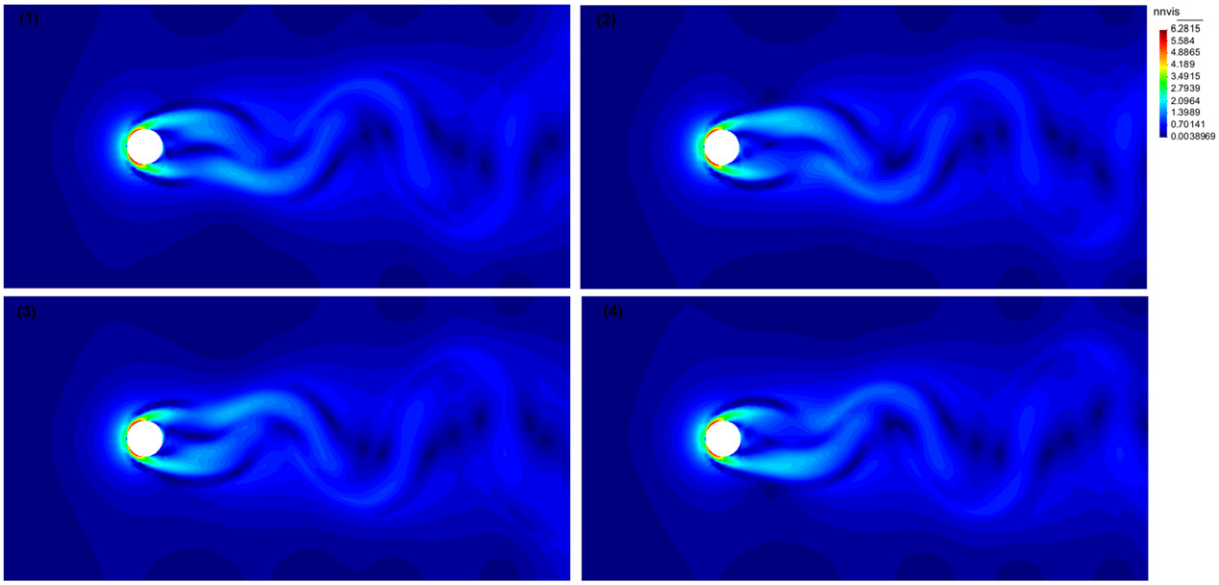

Fig. 13. Viscosity contours, in the cylinder problem, for the case $n = 1.8$ and $\mathrm{Re}_{\mathrm{PL}} = 140$. (For interpretation of the references to color in this figure legend, the reader is referred to the web version of this article.)

in the vicinity of the cylinder of 6.28 (314 times greater than 0.02). The problem is thus convection dominated and with a high non-linear variation in the viscosity, and the numerical formulations proposed are able to cope with this problem, which is what we intend to demonstrate in this work.

4.4. Tangential stresses over boundary walls

The evaluation of stresses over boundaries is an important need in some biomechanical applications that involve blood flow, for example (see [41,42]). In order to evaluate the performance of the three-field formulation to compute these stresses, and compare it with the corresponding two-field method, we will present the results obtained in the calculation of shear stresses first on a 2D straight pipe and then over curved walls in two 3D examples, that we shall refer

Table 9
Blood properties with the Carreau–Yasuda model (SI units).

Fluid type	μ_0	μ_∞	λ	n	a	ρ
Shear-thinning	0.022	0.0022	0.392	0.11	0.624	1410

Table 10
Meshes used in the shear stresses problems.

Meshes	Straight pipe	Arterial stenosis	Arterial elbow
M1	2111n/4000e	97517n/583033e	112331n/524981e
M2	8221n/16000e	168770n/1150852e	175273n/838841e
M3	22345n/43956e		

to as arterial stenosis and arterial elbow. In all the results, the blood properties of a Carreau–Yasuda model with the parameters shown in Table 9 are used. Since our intention is to compare the two-field and the three-field approaches, the OSS method will be used in all cases.

The number of elements and mesh nodes used in each problem are indicated in Table 10. Unstructured meshes of linear triangles in 2D and linear tetrahedra in 3D are used. Also, the Reynolds numbers that define each problem are $\mathrm{Re} = 2000$ in the straight pipe, $\mathrm{Re} = 113$ in the arterial stenosis and $\mathrm{Re} = 227$ in the arterial elbow.

Let us start discussing the results obtained for the 2D straight pipe. Fig. 14 shows the distribution of shear stresses σ_{xy}. A parabolic velocity profile is prescribed at the inlet of the pipe, and it varies along its axis until reaching the constant value corresponding to the constitutive model. In Fig. 14 it is observed that the results obtained with mesh M3 (with 43,956 elements) using the two-field approach are almost the same as those obtained with mesh M2 (with 16,000 elements) using the three-field approach. The gain in accuracy using the three-field formulation is clearly demonstrated. Note that mesh M2 with the three-field approach has $8221 \times 6 = 49{,}326$ degrees of freedom, whereas mesh M3 with the two-field one has $22{,}345 \times 3 = 67{,}035$ degrees of freedom, 35% more than the former.

The extension to the 3D case is shown in two problems. The first corresponds to an arterial stenosis occlusion of 50% and the second an arterial elbow, both represented in Fig. 15. Fig. 16 shows the contour of velocity magnitude and pressure, both for the stenosis and the elbow problems. These contours are plotted for the mid planes in both cases.

In order to compare the stress calculation in the two-field and the three-field formulations, we will plot the modulus of the stress along a line. In the stenosis problem, this line will be the intersection of the boundary with the mid plane between the two cross sections indicated in Fig. 15(a), so that the stenosis is located approximately at the middle of this line. In the case of the elbow, this line is the external intersection of the boundary with the mid plane between the two cross sections closest to the elbow indicated in Fig. 15(b). In both cases, the curves to plot the stresses will be developed in a straight line.

Results are shown in Fig. 17. In both problems we have used meshes M1 and M2 for the two-field approach and only mesh M1 for the three-field formulation (see Table 10 for the description of these meshes). It is clearly observed that the results with M1 in the three-field approach are similar to those obtained with M2 in the two-field one. In fact, in the stenosis problem the three-field formulation is even able to reproduce a higher stress peak at the stenosis with mesh M1 than the two-field one with mesh M2.

The better accuracy of the three-field approach over the two-field one is a general trend that we attribute to the fact that the former has more degrees of freedom than the latter, even if the interpolation order and consequently the convergence rates are the same. The continuous solution can be approximated with better accuracy simply because the constraint $\boldsymbol{\sigma}_h = 2\eta\nabla^s \boldsymbol{u}_h$ at interpolation level is replaced by an additional equation for the stresses.

Obviously, the computational cost of the three-field approach is much higher than for the two-field one. For equal interpolation for all variables, six additional degrees of freedom per node are required in the 3D case. To partially alleviate this problem, one can design block-iterative schemes to segregate the calculation of the stresses from that of the velocity and the pressure, as those proposed in [43] for the strain–displacement approach in solid mechanics. Whether the additional computational cost is compensated or not by the increased accuracy observed is problem dependent, and depends also on the variables we wish to analyze, as this example has demonstrated. Without using any stress segregation scheme, the calculation using the two-field formulation on mesh M3 took 18% more CPU time than

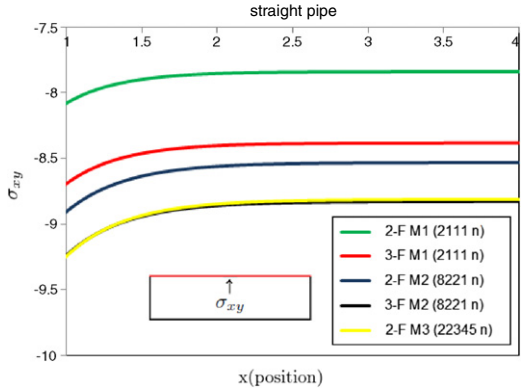

Fig. 14. Shear stress (σ_{xy}) in the straight pipe using the Carreau–Yasuda blood flow.

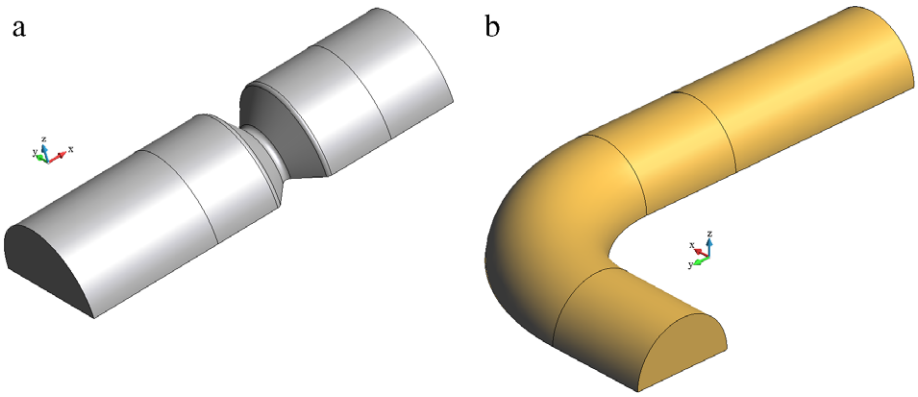

Fig. 15. Schematic representation of tridimensional problems: (a) arterial stenosis and (b) vessel elbow.

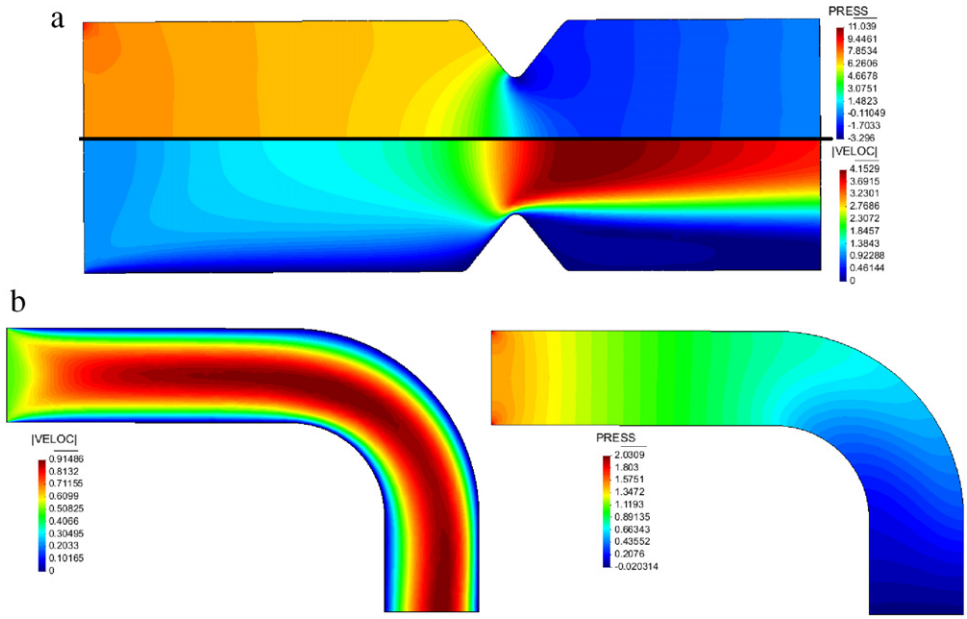

Fig. 16. Contour of pressure (PRESS) and velocity magnitude (VELOC) in the stenosis problem (a) and in the elbow problem (b). Both cases correspond to the mid section. (For interpretation of the references to color in this figure legend, the reader is referred to the web version of this article.)

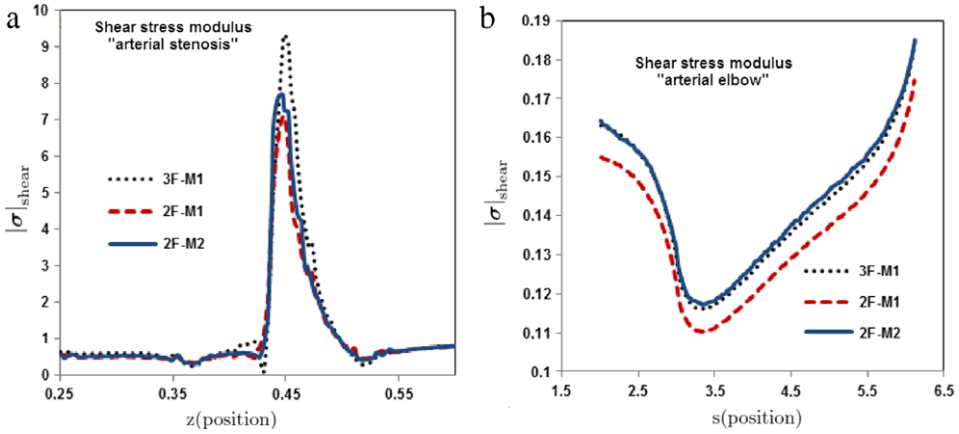

Fig. 17. Shear stress modulus in the arterial stenosis problem (a) and in the vessel elbow problem (b).

the calculation using the three-field one on mesh M2, for a similar accuracy, but using mesh M2 in both cases the former took 56% less CPU time. However, the interest of the three-field approach relies on applications where it is not a choice, but a need, as in the case of viscoelastic flows.

5. Conclusions

In this paper we have proposed two stabilized numerical formulations (ASGS and OSS) of SGS type for the three-field (stress–velocity–pressure) Navier–Stokes problem with nonlinear viscosity models. It has been tested numerically that both formulations have optimal convergence properties for linear and quadratics elements, also evidencing a clear reduction in the L^2-norm of the error when approximating a problem with analytical solution with respect to the two-field (velocity–pressure) formulation. Likewise, for a fixed mesh the OSS method tends to perform better than the ASGS approach, introducing less numerical dissipation.

The proposed schemes were tested in different numerical test cases available in the literature. The range of $100 \leq \mathrm{Re}_{\mathrm{PL}} \leq 5000$ was considered in the mixing cavity problem with non-Newtonian power-law and Carreau–Yasuda fluids, and the range of $40 \leq \mathrm{Re}_{\mathrm{PL}} \leq 140$ in the classical flow over a cylinder. In both cases, results compare satisfactorily with reference solutions found in the literature, both in the location of primary vortexes and in the value of macroscopic parameters, namely the Strouhal number and the drag and lift coefficients, for a power-law fluid with power index in the range $0.4 \leq n \leq 1.8$. In the calculation of shear stresses over the boundaries of the domain the three-field formulation is superior to its two-fields counterpart with a fixed mesh.

The numerical results presented serve to demonstrate the feasibility of the finite element formulation proposed to approximate the three-field Navier–Stokes problem, both in situations in which the viscosity is non-linear and in convection dominated flows, using *equal interpolation for all the unknowns*. In the problem considered, introducing the stresses as unknowns is not mandatory. However, there are situations in which this is a must, notably in the case of viscoelastic flows. The methods proposed are promising tools to attempt this problem.

Acknowledgments

E. Castillo gratefully acknowledges the support received from CONICYT (Programa de Formación de Capital Humano Avanzado/Becas-Chile Folio 72120080), and from the Universidad de Santiago de Chile. R. Codina gratefully acknowledges the support received from the Catalan Government through the ICREA Acadèmia Research Program.

References

[1] T.K. Bandyopadhyay, S.K. Das, Non-Newtonian pseudoplastic liquid flow through small diameter piping components, J. Petroleum Sci. Eng. 55 (1–2) (2007) 156–166.

[2] M.A. Cruchaga, D.J. Celentano, R.W. Lewis, Modelling of twin-roll strip casting processes, Commun. Numer. Methods Eng. 19 (8) (2003) 623–635.

[3] N. Moraga, E. Castillo, C. Garrido, Non Newtonian annular alloy solidification in mould, Heat Mass Transf. 48 (8) (2012) 1415–1424.
[4] R.A. Lemus-Mondaca, N.O. Moraga, J. Riquelme, Unsteady 2D conjugate natural non-Newtonian convection with non-Newtonian liquid sterilization in square cavity, Int. J. Heat Mass Transfer 61 (0) (2013) 73–81.
[5] B.M. Johnston, P.R. Johnston, S. Corney, D. Kilpatrick, Non-Newtonian blood flow in human right coronary arteries: steady state simulations, J. Biomech. 37 (5) (2004) 709–720.
[6] R.B. Bird, W.E. Stewart, E.N. Lightfoot, Transport Phenomena, second ed., Wiley, New York, 2002.
[7] P.J. Carreau, R.P. Chhabra, Rheology of Polymeric Systems: Principles and Applications, second ed., Hanser, Munich, 1997.
[8] J.-B. Zhang, Z.-B. Kuang, Study on blood constitutive parameters in different blood constitutive equations, J. Biomech. 33 (3) (2000) 355–360.
[9] T.S. Montgomery, W. MacKnight, Introduction to Polymer Viscoelasticity, third ed., Wiley, New Jersey, 2005.
[10] F. Brezzi, M. Fortin, Variational formulations and finite element methods, in: F. Brezzi, M. Fortin (Eds.), Mixed and Hybrid Finite Element Methods, in: Springer Series in Computational Mathematics, vol. 15, Springer, New York, 1991, pp. 1–35.
[11] R. Codina, Finite element approximation of the three-field formulation of the Stokes problem using arbitrary interpolations, SIAM J. Numer. Anal. 47 (1) (2009) 699–718.
[12] D. Sandri, Analyse d'une formulation à trois champs du problème de Stokes, ESAIM Math. Model. Numer. Anal. 27 (7) (1993) 817–841.
[13] V. Ruas, An optimal three-field finite element approximation of the Stokes system with continuous extra stresses, Jpn. J. Ind. Appl. Math. 11 (1) (1994) 113–130.
[14] M. Fortin, A. Fortin, A new approach for the FEM simulation of viscoelastic flows, J. Non-Newton. Fluid Mech. 32 (3) (1989) 295–310.
[15] J. Marchal, M. Crochet, A new mixed finite element for calculating viscoelastic flow, J. Non-Newton. Fluid Mech. 26 (1) (1987) 77–114.
[16] M. Fortin, R. Pierre, On the convergence of the mixed method of Crochet and Marchal for viscoelastic flows, Comput. Methods Appl. Mech. Engrg. 73 (3) (1989) 341–350.
[17] A.N. Brooks, T.J. Hughes, Streamline upwind/Petrov–Galerkin formulations for convection dominated flows with particular emphasis on the incompressible Navier–Stokes equations, Comput. Methods Appl. Mech. Engrg. 32 (1–3) (1982) 199–259.
[18] T.J. Hughes, L.P. Franca, G.M. Hulbert, A new finite element formulation for computational fluid dynamics: VIII the Galerkin/least-squares method for advective-diffusive equations, Comput. Methods Appl. Mech. Engrg. 73 (2) (1989) 173–189.
[19] J. Douglas Jr., T. Russell, Numerical methods for convection-dominated diffusion problems based on combining the method of characteristics with finite element or finite difference procedures, SIAM J. Numer. Anal. 19 (5) (1982) 871–885.
[20] J. Donea, A Taylor–Galerkin method for convective transport problems, Internat. J. Numer. Methods Engrg. 20 (1) (1984) 101–119.
[21] R. Codina, Comparison of some finite element methods for solving the diffusion–convection–reaction equation, Comput. Methods Appl. Mech. Engrg. 156 (1–4) (1998) 185–210.
[22] T.J. Hughes, G.R. Feijóo, L. Mazzei, J.-B. Quincy, The variational multiscale method-a paradigm for computational mechanics, Comput. Methods Appl. Mech. Engrg. 166 (1–2) (1998) 3–24.
[23] R. Codina, Stabilization of incompressibility and convection through orthogonal sub-scales in finite element methods, Comput. Methods Appl. Mech. Engrg. 190 (13–14) (2000) 1579–1599.
[24] S.S. Mendu, P. Das, Flow of power-law fluids in a cavity driven by the motion of two facing lids — a simulation by lattice Boltzmann method, J. Non-Newton. Fluid Mech. 175–176 (0) (2012) 10–24.
[25] V.K. Patnana, R.P. Bharti, R.P. Chhabra, Two-dimensional unsteady flow of power-law fluids over a cylinder, Chem. Eng. Sci. 64 (12) (2009) 2978–2999.
[26] O.C. Zienkiewicz, R.L. Taylor, P. Nithiarasu, The Finite Element Method for Fluid Dynamics, vol. 3, sixth ed., Elsevier, Butterworth-Heinemann, 2005.
[27] J. Bonvin, M. Picasso, R. Stenberg, GLS and EVSS methods for a three-field Stokes problem arising from viscoelastic flows, Comput. Methods Appl. Mech. Engrg. 190 (29–30) (2001) 3893–3914.
[28] J.S. Howell, Dual-mixed finite element approximation of Stokes and nonlinear Stokes problems using trace-free velocity gradients, J. Comput. Appl. Math. 231 (2) (2009) 780–792.
[29] R. Codina, A stabilized finite element method for generalized stationary incompressible flows, Comput. Methods Appl. Mech. Engrg. 190 (20–21) (2001) 2681–2706.
[30] R. Codina, Stabilized finite element approximation of transient incompressible flows using orthogonal subscales, Comput. Methods Appl. Mech. Engrg. 191 (39–40) (2002) 4295–4321.
[31] T.J. Hughes, Multiscale phenomena: Green's functions, the Dirichlet-to-Neumann formulation, subgrid scale models, bubbles and the origins of stabilized methods, Comput. Methods Appl. Mech. Engrg. 127 (1–4) (1995) 387–401.
[32] R. Codina, J. Principe, O. Guasch, S. Badia, Time dependent subscales in the stabilized finite element approximation of incompressible flow problems, Comput. Methods Appl. Mech. Engrg. 196 (2007) 2413–2430.
[33] R. Codina, J. Principe, Dynamic subscales in the finite element approximation of thermally coupled incompressible flows, Internat. J. Numer. Methods Fluids 54 (2007) 707–730.
[34] S. Badia, R. Codina, On a multiscale approach to the transient Stokes problem: dynamic subscales and anisotropic space–time discretization, Appl. Math. Comput. 207 (2) (2009) 415–433.
[35] R. Codina, Analysis of a stabilized finite element approximation of the Oseen equations using orthogonal subscales, Appl. Numer. Math. 58 (3) (2008) 264–283.
[36] M. Avila, J. Principe, R. Codina, A finite element dynamical nonlinear subscale approximation for the low Mach number flow equations, J. Comput. Phys. 230 (22) (2011) 7988–8009.
[37] J. Principe, R. Codina, F. Henke, The dissipative structure of variational multiscale methods for incompressible flows, Comput. Methods Appl. Mech. Engrg. 199 (2010) 791–801.
[38] Y. Saad, M. Schultz, GMRES: a generalized minimal residual algorithm for solving nonsymmetric linear systems, SIAM J. Sci. Stat. Comput. 7 (3) (1986) 856–869.

[39] R.P. Bharti, R.P. Chhabra, V. Eswaran, Steady flow of power law fluids across a circular cylinder, Can. J. Chem. Eng. 84 (4) (2006) 406–421.
[40] A.A. Soares, J.M. Ferreira, R.P. Chhabra, Flow and forced convection heat transfer in crossflow of non-Newtonian fluids over a circular cylinder, Ind. Eng. Chem. Res. 44 (15) (2005) 5815–5827.
[41] D. Wang, J. Bernsdorf, Lattice Boltzmann simulation of steady non-Newtonian blood flow in a 3D generic stenosis case, Comput. Math. Appl. 58 (5) (2009) 1030–1034.
[42] J. Chen, X.-Y. Lu, W. Wang, Non-Newtonian effects of blood flow on hemodynamics in distal vascular graft anastomoses, J. Biomech. 39 (11) (2006) 1983–1995.
[43] M. Cervera, M. Chiumenti, R. Codina, Mixed stabilized finite element methods in nonlinear solid mechanics. part I: formulation, Comput. Methods Appl. Mech. Engrg. 199 (2010) 2559–2570.